PAPER

Designing an electromechanical metamaterial beam with arbitrary decoupled defect modes for multi-band wave localization

IOP Publishing Smart Materials and Structures
Smart Mater. Struct. **34** (2025) 035015 (21pp) https://doi.org/10.1088/1361-665X/adb35e

Designing an electromechanical metamaterial beam with arbitrary decoupled defect modes for multi-band wave localization

Yupei Jian[1], Lihua Tang[2], Deqing Huang[1], Hesheng Han[2], Weiqun Liu[3,*] and Guobiao Hu[4,*]

[1] School of Electrical Engineering, Southwest Jiaotong University, Chengdu, Sichuan 610031, People's Republic of China
[2] Department of Mechanical and Mechatronics Engineering, The University of Auckland, Auckland 1010, New Zealand
[3] School of Mechanical Engineering, Southwest Jiaotong University, Chengdu, Sichuan 610031, People's Republic of China
[4] Internet of Things Thrust, The Hong Kong University of Science and Technology (Guangzhou), Guangzhou, Guangdong 511400, People's Republic of China

E-mail: weiqunliu@home.swjtu.edu.cn and guobiaohu@hkust-gz.edu.cn

Received 4 December 2024, revised 21 January 2025
Accepted for publication 5 February 2025
Published 17 February 2025

Abstract

Defective phononic crystals (PnCs) and metamaterials have gained considerable attention for applications in waveguiding, energy harvesting, and sensing. Despite the increasing interest, traditional defective PnCs/metamaterials are typically restricted to single or dual defect bands, with narrow tunable ranges constrained by the bandgap width. Instead of structural defects, this study introduces an approach to achieve arbitrary decoupled defect modes in defective piezoelectric metamaterial via electrically controlled defects, enabling flexible wave localization across multiple frequency bands. Specifically, we design multiple bandgaps in piezoelectric metamaterials by paralleling unit cells with higher-order resonant circuits that include 'current-flowing' branches and consequently propose a multi-bandgap decoupling tuning method. Based on this, a conjecture that adjusting the inductance of a single cell can produce defect bands in all bandgaps is proposed. To accurately predict defect bands, harmonic responses, and wave modes, the spectral element method, incorporating the Timoshenko beam unit, is used to describe the dynamic properties of the metamaterial, which are further validated by finite element analysis. The influence of electrical open-circuit and short-circuit conditions on defect-mode frequencies, alongside the frequency-dependent properties of the energy localization effect are investigated. Results confirm that an arbitrary number of defect bands at specific frequencies can be achieved by tuning the defective cell's electrical impedance, with each band's tunability and corresponding energy-localized behavior functioning independently. The proposed approach uniquely enables multi-band wave localization with a single-point defect, offering a significant advantage over conventional methods requiring multiple structural defects, and opening new avenues for programmable wave localization in complex vibration scenarios.

* Authors to whom any correspondence should be addressed.

Keywords: defective piezoelectric metamaterial, electrically controlled defect,
multi-band wave localization, arbitrary decoupled defect modes, higher-order resonant circuit

1. Introduction

Manipulating the amplitude/propagation direction of waves has been a fundamental goal in engineering structures [1]. Phononic crystals (PnCs) [2, 3], designed from artificial microstructural units, have opened new frontiers in wave-based functional materials. The unconventional approach of controlling wave propagation through Bragg scattering (BS) bandgap shows great promise for applications such as vibration suppression [4, 5], wave filtering [6, 7], sensing and detection [8, 9], and elastic mirrors [10]. Recent developments in periodicity theory have led to the emergence of metamaterial, enabling the formation of local resonance (LR) bandgaps at lattice scales well below the wavelength [11], and advancing subwavelength control of elastic/acoustic waves.

An important branch of wave manipulation in PnCs/metamaterials is spatial localization and local wave energy amplification through defects [12, 13]. It is known that bandgap in PnCs/metamaterials prevents the transmission of incident waves. However, introducing defects breaks the perfect periodicity, thereby disrupting the bandgap in certain frequency ranges and creating passbands (defect bands) that allow waves of specific frequencies to propagate. With the bandgap still restricting wave transmission in defect-free regions, waves at specific frequencies 'flow' into the defect, forming standing waves and amplifying the local amplitude—a phenomenon known as defect mode [14]. Defect modes in PnCs and metamaterials are typically formed in BS bandgaps and LR bandgaps, respectively, and both have been widely studied.

In PnCs, defects can be created by altering the geometric or material properties of specific unit cells [15]. Shelke *et al* [16] studied the ultrasonic waveguide properties of a defective PnC consisting of a square array of cylindrical rods in an air matrix by removing some of the cylindrical rods. Sound waves at defect-mode frequencies can propagate along defects with minimal loss, demonstrating potential for narrowband filtering. Similarly, Shao *et al* [17] investigated the energy amplification properties of elastic waves in cylindrical rod arrays containing line defects, illustrating its application for energy harvesting. Moving beyond simple removal of units, Park *et al* [18] designed a defective PnC with an octagonal hole in each unit cell. The intricate geometry of cells provides greater flexibility for defect design, leading to improved energy amplification in the defect region. Recent advancements in intelligent algorithm-assisted inverse designs have further customized wave localization behavior in defective PnCs [19–22]. It is worth noting that defect-mode frequencies in defective PnCs are typically in the upper kilohertz range due to the BS mechanism [23], limiting their application to the high-frequency spectrum. Metamaterials, however, provide a solution. Generally, defects in metamaterials are introduced by modifying the resonance properties of the unit cells, leading to defect modes within the LR bandgap, thereby significantly reducing their formation frequency. Oudich and Li [24] presented a defective metamaterial plate placed in an acoustic field, featuring an array of mass-spring resonators integrated into the plate. By modifying the properties of selected resonator units, a defect mode is produced within the LR bandgap around 500 Hz. Katch *et al* [25] examined the effect of varying partial resonators' stiffness on the defect mode properties in metamaterial beams with periodically arranged mass-spring resonators. The findings are valuable for applications such as structural defect detection. In addition to spring-mass resonators, other resonators with defects, such as elastically wrapped scatterers [26], Helmholtz cavities [27, 28], and piezoelectric resonance units [29–31], have been explored to induce defect modes in metamaterials, all shown effective low-frequency spatial localization.

Understanding that defect bands in PnCs/metamaterials are typically flat, exhibiting narrowband characteristics due to their near-zero group velocity [32, 33]. The single defect mode created in the abovementioned studies is suboptimal for practical applications with broadband spectrum. To address this, researchers have proposed various design strategies to expand the operational frequency of defect modes, which can be broadly classified into two categories. The first category focuses on creating multiple defect modes in PnCs/metamaterials. For instance, Jo *et al* [34] proposed double-defect PnC with circular hole-type unit cells. Two coupled defect bands are formed within the BS bandgap by leveraging the splitting effect of the defect modes in a double-defect configuration, where the spatial spacing between the defects influences both defect bands. Further, they investigated PnCs with widely spaced double defects, incorporating a gradient in the cell size around each defect to successfully decouple the two defect modes [35]. However, the number of defect modes that can be created is limited, as excessive structural defects would destroy the bandgap. Moreover, the defect modes created in this way are all formed within the same bandgap, restricting their operational bandwidth. Another effective approach, beyond increasing the number of structural defects, is to skillfully form defect modes within multiple bandgaps. Xiao *et al* [36] designed a Helmholtz resonator-based defective metamaterial, successfully generating defect modes within the two bandgaps formed by the mechanical and acoustic resonances of Helmholtz resonators.

The second category focuses on achieving tunable/programmable defect modes to address broadband vibrational challenges. Specifically, by integrating materials such as piezoelectric materials [37], electromagnetic materials [38], and thermosensitive materials [39] into PnCs/metamaterials, their multi-field coupling properties are exploited to modify

lattice geometry and material features and enable defect band tunability. For instance, Deng *et al* [40] integrate magnetostrictive rods within defective PnCs to achieve defect band frequency shifts of approximately 1% and 5%, respectively. Jo *et al* [41] attached a piezoelectric patch shunted with negative capacitance circuits at the defect in PnCs, utilizing the stiffness adjustment capability of the negative capacitance circuit to achieve tunable defect bands. Thomes *et al* [42] examined the spatio-temporal tunability of defect modes in piezoelectric metamaterials with shunted inductive circuits. The authors also investigated the rainbow effect of defect modes in grading piezoelectric metamaterials, which exhibit frequency-space selective properties [43]. Although the above approaches allow for some tunability of defect bands, a major limitation is that the defect bands are formed in a single bandgap and their tuning range is limited by the bandgap width.

These research gaps motivate us to explore whether it is feasible to achieve arbitrary decoupled defect modes using the tunable properties of piezoelectric metamaterials. Here, 'arbitrary' refers to freely specifying both the number and frequency of defect modes, while 'decoupling' allows independent tuning of each mode's frequency and wave localization, enabling multiple defect modes to function without interference. To this end, we propose a scenario where a single piezoelectric defect can induce multiple defect bands in different LR bandgaps. A higher-order resonant circuit comprising current-flowing branches is employed to generate multiple bandgaps in piezoelectric metamaterials. Given the narrowband properties of defect bands, we develop an spectral element method (SEM) analytical model, based on Timoshenko beam theory and Hamilton's principle, to capture the bandgap behavior accurately. Leveraging negative stiffness theory and the open-circuit features of the current-conducting branches, we establish a framework for decoupling bandgaps, proving a basis for independently tuning multiple defect bands.

The key distinction of this design from existing approaches lies in its circuit-controlled defect bands, enabling arbitrary multi-band wave localization with only a single structural defect. It overcomes traditional methods that rely on structural defects, thereby greatly enhancing the applicability of defect modes. Furthermore, the programmable nature of piezoelectric elements suggests that future integration with digital circuits and sensing modules could enable the proposed design to adaptively respond to environmental changes, allowing for customized control over the number, frequency, and spatial positioning of wave localization. This advancement offers a novel solution for wave guiding, sensing, and structural health monitoring in complex vibration environments.

The paper is organized as follows: section 2 details the structure and circuit configuration of the defective piezoelectric metamaterials. section 3 outlines the methodology for defect band and harmonic response analyses using the SEM based on Timusinko theory. Section 4 presents a multi-bandgap decoupling tuning method for the higher-order resonant circuits. Section 5 commences with a comprehensive analysis of the defect modes induced by a first-order resonant circuit, followed by a demonstration of the decoupling of the double defect modes under the higher-order resonant circuits. Furthermore, additional examples are provided to showcase the arbitrary decoupled defect modes. Finally, concluding remarks are summarized in section 6.

2. Design of defective metamaterials with arbitrary decoupled defect modes

The proposed defective metamaterials with arbitrary decoupled defect modes are comprised of one-dimensional piezoelectric metamaterial beams incorporating piezoelectric defects. Section 2.1 describes the physical structure of the defective piezoelectric metamaterial. The deliberate modification of the circuitry in a unit cell introduces a point defect in the metamaterial. Section 2.2 presents the electrical circuit configuration and highlights the advantages of using the higher-order resonant circuit consisting of 'current-flowing' branches to create multiple decoupled bandgaps, which are the basis of arbitrary decoupled defect modes.

2.1. Overview of the defective piezoelectric metamaterial

Figure 1 shows the schematic of the defective piezoelectric metamaterial beam with arbitrary decoupled defect modes. This elastic beam consists of a three-layer structure in which two piezoelectric layers, polarized in the same direction along the z-axis, cover the top and bottom surfaces of the substrate layer. The repeating pattern consisting of k unit cells (unit cells are distinguished by j, and $j = 1, 2, \ldots, k$) is realized by periodically arranged electrode pairs on the piezoelectric layers. Each electrode pair is connected to an external resonant circuit with a general impedance $Z_j(s)$, which describes the relation between voltage $v_p(t)$ and current $i_p(t)$. Consequently, unit cells are electrically independent, but the boundaries of adjacent cells share the same mechanical degrees of freedom (DOFs). In this study, the periodicity of metamaterial is intentionally broken by modifying the general impedance in the jth unit cell, resulting in a defect with energy-localized behavior, as indicated in figure 1(a). Figure 1(b) shows the close-up view of the unit cell. In defect-free cells, electrode pairs are connected in parallel with higher-order resonant circuits, whereas in the defective cell (indicated by the yellow electrode), they are connected in parallel with a first-order resonant circuit. The material and geometric properties of the defective piezoelectric metamaterial beam are given in table 1.

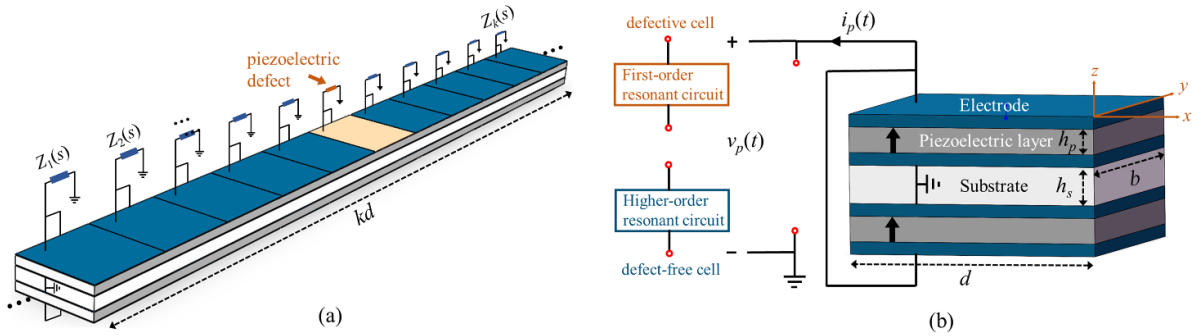

Figure 1. (a) Schematic of a defective piezoelectric metamaterial with arbitrary decoupled defect modes; (b) an enlarged view of the unit cell in which the two electrode pairs are connected in parallel with a resonant circuit. In this case, defect-free cells are connected to a higher-order resonant circuit, while the defective cell is connected to a first-order resonant circuit.

Table 1. Material and geometric properties of the defective piezoelectric metamaterial beam.

Substrate layer—Brass			
Density ρ_s	7165 kg m^{-3}	Cell length d	30 mm
Young's modulus E_s	100 GPa	Cell width b	20 mm
Shear modulus G_s	40 GPa	Cell thickness h_s	1.5 mm
Piezoelectric layer—PZT-5			
Density ρ_p	7800 kg m^{-3}	Cell length d	30 mm
Young's modulus $1/S_{11}^E$	66 GPa	Cell width b	20 mm
Shear modulus $1/S_{55}^E$	21 GPa	Cell thickness h_p	0.4 mm
Permittivity ε_{33}^T	15.93 nF m^{-1}	Piezoelectric constant d_{31}	-19×10^{-9} C/N

2.2. Higher-order resonant circuit for generating multiple decoupled bandgaps

Analogous to the tuned mass damper [44], the jth piezoelectric element with a first-order resonant circuit (typically represented by a resistor-inductor series circuit) acts as an electromechanical resonator. The interaction between these periodically arranged electromechanical resonators and the substrate creates LR bandgaps. The diagram of the first-order resonant circuit with impedance $Z_j^f(s)=R+sL$ is shown in figure 2(a), where the piezoelectric element is modeled as a voltage source V_p in series with a capacitor C_p. It is known that by intentionally varying the inductance of a certain cell, a defect mode induced by piezoelectric defect emerges within the bandgap, with its tunability constrained by the bandgap width [42]. However, this single defect mode limits its applications as bandpass filters/sensors/energy harvesters in broadband vibration scenarios. To extend the operating bandwidth of defect mode, we propose that defect modes can be formed in multiple bandgaps by introducing piezoelectric defects associated with multiple resonant frequencies in the unit cell. This is achieved by connecting a first-order resonant circuit to the defective cell to introduce piezoelectric defects, while higher-order resonant circuits are connected to the defect-free cells to generate multiple bandgaps, as demonstrated in figure 1(b).

In this study, a higher-order resonant circuit [45] consisting of current-flowing branches (orange parts) and resonance branches (green parts), named C-F higher-order resonant circuit for brevity, is utilized to generate multiple decoupled bandgaps. The diagram of the C-F higher-order resonant circuit is shown in figure 2(b). Compared to conventional higher-order resonant circuits, such as the one used in [46], a significant advantage of this circuit lies in the decoupling of different orders of electrical resonance through the incorporation of current-flowing branches, which enables each resonance branch to function independently. To be specific, when the inductor in the ith current-flowing branch is tuned to $\tilde{L}_i=1/\left(\omega_i^2C_i\right), i=1,2,\ldots,n$, the impedance $Z_i^{\mathrm{cf}}(s)$ of the ith current-flowing branch approaches zero (i.e. it behaves at a short circuit) at the operating frequency ω_i. Conversely, at other frequencies, the ith current-flowing branch acts approximately as an open circuit. In other words, the current-flowing branches act as a 'switch', ensuring that each resonant branch operates exclusively around its designed frequency. As an example, we chose $\omega=500\times2\pi$ rad s^{-1} to illustrate how the impedance magnitude $\left|Z^{\mathrm{cf}}(s)\right|$ varies with frequency to demonstrate the switching characteristics of the current-flowing branch, as shown in figure 2(d). It can also be observed from the figure that as the capacitance decreases, the switching characteristics become more pronounced. Another advantage of this switching characteristic is that, due to the decoupling of the individual resonant branches, the other branches can continue to operate normally even when the inductance of one branch is perturbed. Applying the electrical-mechanical

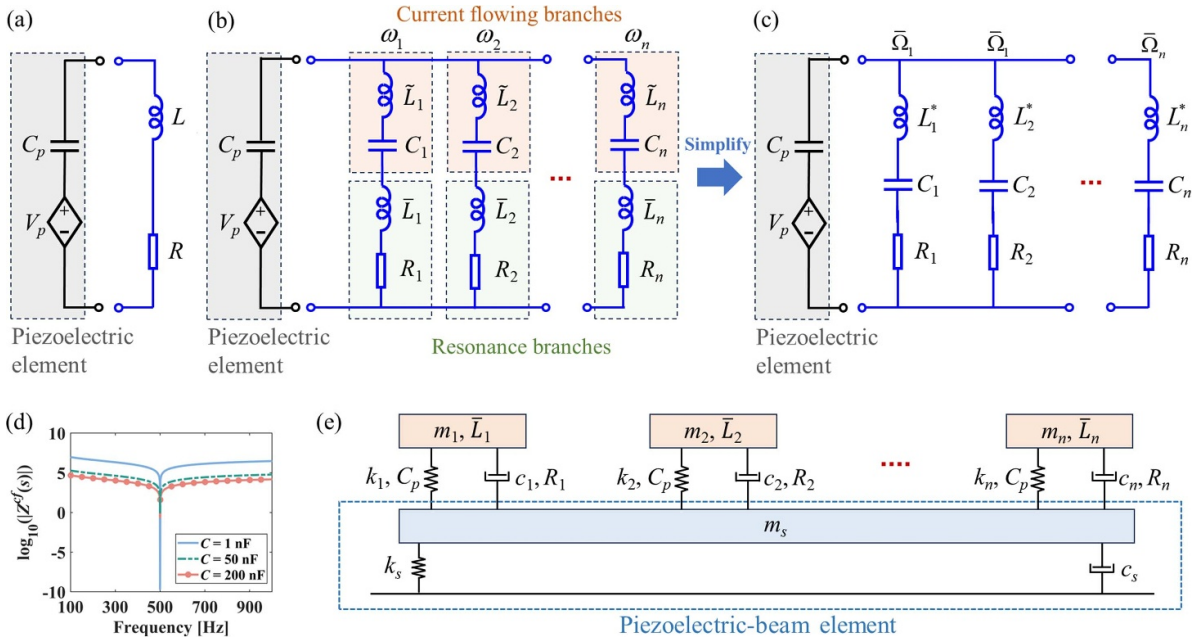

Figure 2. (a) The diagram of the first-order resonant circuit; (b) the diagram of the C-F higher-order resonant circuit with n branches; (c) simplified circuit after integrating inductors $\tilde{L}$ and $\bar{L}$ into L^*; (d) variation of the impedance magnitude of the current-flowing branch with frequency; (e) the equivalent mechanical model of the current under electrical-mechanical analogy.

analogy, the C-F higher-order resonant circuit can be regarded as a multi-DOF vibration absorber consisting of a number of spring-mass blocks connected in parallel, each of which can be individually tuned, as shown in figure 2(e). In this analogy, a piezoelectric-beam element is equated by a mass m_s, stiffness k_s, and damping c_s [46].

Consequently, the method of obtaining multiple independent bandgaps becomes straightforward: By tuning $\bar{L}_i$ in the ith resonance branches to $\bar{L}_i = 1/\left(\bar{\Omega}_i^2 C_p\right)$, multiple bandgaps associated with the desired resonant frequencies, i.e. $\bar{\Omega}_1$, $\bar{\Omega}_2$, …, $\bar{\Omega}_n$, can be generated. To simplify this circuit, inductors $\tilde{L}_i$ and $\bar{L}_i$ in the ith branch can be integrated into a single inductor $L_i^* = \frac{C_p + C_i}{\bar{\Omega}_i^2 C_p C_i}$, as shown in figure 2(c). The total shunt branches impedance, denoted by $Z_j^c(s)$, of the C-F higher-order resonant circuit containing n branches in the jth unit cell can be expressed as:

$$Z_j^c(s) = \frac{1}{\sum_{i=1}^{n} \frac{sC_i}{1 + sR_iC_i + s^2 L_i^* C_i}}. \tag{1}$$

In section 4, we will further compare the differences in bandgap tuning between the C-F higher-order circuit and its conventional counterpart, and propose a multi-bandgap decoupling tuning method.

3. Analytical approaches for defect bands

This section elaborates on the mathematical formulation to facilitate the analysis of piezoelectric metamaterial with a point defect. It commences with introducing the governing equations for the piezoelectric-beam element shunted with the C-F higher-order resonant circuit. Subsequently, the dynamics model of the proposed defective piezoelectric metamaterial is developed using the spectral transfer matrix method (STMM) to perform band structure analysis and the SEM to compute harmonic responses.

3.1. Governing equations

The defect band is normally a narrow passband within bandgaps, necessitating precise modeling to accurately capture its frequency range. Therefore, Timoshenko's beam theory, which accounts for structural shear deformation, is adopted to enhance the predicting accuracy of the defect bands.

The linear constitutive equation describing the elastic and electrostatic relationships of the piezoelectric materials takes the forms [47]:

$$\begin{bmatrix} \sigma_p \\ \kappa_p \\ E_3 \end{bmatrix} \begin{bmatrix} C_{11}^D & 0 & -h_{31} \\ 0 & C_{55}^D & 0 \\ -h_{31} & 0 & \varepsilon_{33}^S \end{bmatrix} = \begin{bmatrix} \varepsilon_p \\ \gamma_p \\ D_3 \end{bmatrix} \tag{2}$$

where σ_p and ε_p denote the longitudinal stress and strain in the x-direction, while κ_p and γ_p denote the shear stress and strain, respectively. E_3 and D_3 denote the dielectric field and electrical displacement in the z-direction, respectively. C_{11}^D and C_{55}^D refer to the elastic stiffness, h_{31} is the piezoelectric constant. ε_{33}^S is the dielectric permittivity at a constant strain. Notably, equation (2) can be reformulated to express strain as a function of stress, resulting in another set of coefficients [48]:

$$S_{11}^E = 1/C_{11}^D + d_{31}^2 \varepsilon_{33}^T,\ S_{55}^E = 1/C_{55}^D,\ \varepsilon_{33}^T = \varepsilon_{33}^S + d_{31}^2/S_{11}^E,$$
$$d_{31} = h_{31}/\left(\varepsilon_{33}^T C_{11}^D\right) \tag{3}$$

where S_{11}^{E} and S_{55}^{E} are elastic compliance constants, ε_{33}^{T} is the dielectric permittivity at constant stress, and d_{31} is the piezoelectric constant.

According to equation (2), the relationship between stress and strain in piezoelectric materials is as follows:

$$\begin{aligned}&\text{piezoeletric material}\begin{cases}\sigma_p = C_{11}^{D}\varepsilon_p - h_{31}D_3\\ \kappa_p = C_{55}^{D}\gamma_p\end{cases}\\ &\text{substrate material}\begin{cases}\sigma_s = E_s\varepsilon_s\\ \kappa_s = G_s\gamma_s\end{cases}.\end{aligned} \tag{4}$$

The longitudinal and shear stress-strain relationships for the substrate materials are also given in equation (4), where E_s and G_s are the elastic stiffness constants. Additionally, under the small deflection assumption, the strain components in piezoelectric and substrate materials can be expressed in terms of the transverse and rotational displacements, $w\,(x,\,t)$ and $\phi\,(x,t)$, as follows:

$$\begin{cases}\varepsilon_p = -\dfrac{\partial\phi\,(x,t)}{\partial x}y\\ \gamma_p = \phi\,(x,t) - \dfrac{\partial w\,(x,t)}{\partial x}\end{cases}\quad\begin{cases}\varepsilon_s = -\dfrac{\partial\phi\,(x,t)}{\partial x}y\\ \gamma_s = \phi\,(x,t) - \dfrac{\partial w\,(x,t)}{\partial x}\end{cases} \tag{5}$$

To derive the governing equation of the piezoelectric-beam element, the extended Hamilton's principle is utilized as follows [49]:

$$\int_{t_1}^{t_2}\left(\delta T_{\text{kinetic}} - \delta V_{\text{potential}} + \delta W_{\text{virtual}}\right)\mathrm{d}t = 0 \tag{6}$$

where T_{kinetic} and $V_{\text{potential}}$ represent the total kinetic and potential energy, and $\delta W_{\text{virtual}}$ denotes the virtual work done by the non-conservative forces. δ is the variational operator, and $\delta T_{\text{kinetic}}$ is denoted as the variant of T_{kinetic}. The total potential energy can be written as

$$\begin{aligned}V_{\text{potential}} = \frac{1}{2}\Bigg\{&\int_{V_{\text{sub}}}\left(\sigma_s\varepsilon_s + \kappa_s\gamma_s\right)\mathrm{d}V_{\text{sub}} + \int_{V_{\text{piezo}}}\left(\sigma_p\varepsilon_p + \kappa_p\gamma_p\right.\\ &\left.+E_3D_3\right)\mathrm{d}V_{\text{piezo}}\Bigg\}\end{aligned} \tag{7}$$

where V_{sub} and V_{piezo} are volume integral operators for the substrate and piezoelectric materials, respectively. The total kinetic energy is expressed as follows,

$$T_{\text{kinetic}} = \frac{1}{2}\int_{x=0}^{d}\left\{\rho A\left(\frac{\partial w\,(x,t)}{\partial t}\right)^2 + \int_{x=0}^{d}\rho I\left(\frac{\partial\phi\,(x,t)}{\partial t}\right)^2\right\}\mathrm{d}x \tag{8}$$

where $\rho A = b(\rho_s + 2\rho_p)$, $\rho I = \rho_s I_s + 2\rho_p(I_p + bh_p h_{pc})$. $I_s = bh_s^2/12$ and $I_p = bh_p^2/12$. $h_{pc} = \left((h_s + h_p)/2\right)^2$. ρ_s and ρ_p denote the density of the substrate and piezoelectric materials. For the bimorph piezoelectric-beam element under considering in-parallel connection configuration, the virtual work $\delta W_{\text{virtual}}$ done by the external force, moment, and applied electric field, is given by

$$\begin{aligned}\delta W_{\text{virtual}} = &\int_{x=0}^{d}\tilde{F}\delta w\,(x,t)\mathrm{d}x + \int_{x=0}^{d}\tilde{M}\delta\phi\,(x,t)\mathrm{d}x\\ &+2\int_{x=0}^{d}bv_p\,(t)\,\delta D_3\mathrm{d}x\mathrm{d}x\end{aligned} \tag{9}$$

where $\tilde{F}$ and $\tilde{M}$ denote the external force and moment. $v_p(t)$ is the voltage across the piezoelectric elements. Substituting equations (4), (5), (7)–(9) into Hamilton's principle equation (6), and temporally ignoring the $\tilde{F}$and $\tilde{M}$ terms, the governing equations of the piezoelectric-beam element are [50]:

$$\begin{cases}\rho A\dfrac{\partial^2 w\,(x,t)}{\partial t^2} + GA\left[\dfrac{\partial\phi\,(x,t)}{\partial x} - \dfrac{\partial^2 w\,(x,t)}{\partial x^2}\right] = 0\\ \rho I\dfrac{\partial^2\phi\,(x,t)}{\partial t^2} + GA\left[\phi\,(x,t) - \dfrac{\partial w\,(x,t)}{\partial x}\right] - EI\dfrac{\partial^2\phi\,(x,t)}{\partial x^2} = 0\\ \dfrac{h_{pc}h_{31}}{\varepsilon_{33}^{S}}\dfrac{\partial\phi\,(x,t)}{\partial x} + \dfrac{v_p\,(t)}{h_p\varepsilon_{33}^{S}} + D_3 = 0\end{cases} \tag{10}$$

where $EI = E_sI_s + 2C_{11}^{D}\left(I_p + bh_ph_{pc}\right) - 2bh_ph_{pc}h_{31}^2/\varepsilon_{33}^{S}$ and $GA = bh_sG_s + 2bh_p/S_{55}^{E}$. For the bimorph piezoelectric-beam element in a parallel connection configuration, as shown in figure 1(b), the relationship between charge and electric displacement is given by:

$$q\,(t) = 2b\int_{x=0}^{d}D_3\mathrm{d}x. \tag{11}$$

Substituting equation (11) into the third expression of equation (10), and combining it with the relation $i_p\,(t) = \frac{\mathrm{d}q(t)}{\mathrm{d}t}$, the coupled electric field-displacement governing equation is further expressed as

$$i_p\,(t) + \left[C_p\frac{dv_p\,(t)}{dt} - \theta\left(\frac{\partial\phi\,(d,t)}{\partial t} - \frac{\partial\phi\,(0,t)}{\partial t}\right)\right] = 0 \tag{12}$$

where $C_p = 2\varepsilon_{33}^{S}bd/h_p$ is the inherent capacitance of the piezoelectric element, and $\theta = 2bh_{pc}d_{31}/S_{11}^{E}$is the electromechanical coupling coefficient.

3.2. Piezoelectric beam spectral element (PBSE)

In this subsection, the PBSE of the piezoelectric metamaterial with C-F higher-order resonant circuits is developed by the SEM. The PBSE with nodes 1 and 2 is shown in figure 3, where W_1, W_2 and Φ_1, Φ_2 denote the transverse and rotational displacements at nodes 1 and 2, respectively, while M_1, M_2, and Q_1, Q_2 represent the bending moment and shear force at nodes 1 and 2, respectively.

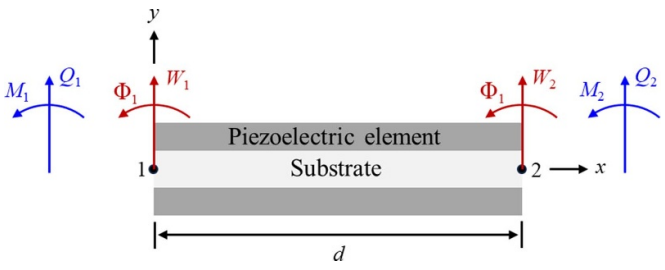

Figure 3. Piezoelectric beam spectral element in the local coordinate system.

Subsequently, the dynamic behavior of the metamaterial can be obtained by assembling the PBSE. The SEM is particularly suitable for modeling periodic structures such as metamaterials due to its advantages of reduced element numbers and high accuracy of frequency-domain results [51].

The general solutions to the governing equations equation (12) can be assumed by

$$\begin{Bmatrix} w(x,t) \\ \phi(x,t) \end{Bmatrix} = \begin{Bmatrix} W(x,\omega)\, e^{\mathrm{i}\omega t} \\ \Phi(x,\omega)\, e^{\mathrm{i}\omega t} \end{Bmatrix} \tag{13}$$

where $W(x,\omega)$ and $\Phi(x,\omega)$ are the spectral components of the transverse and rotational displacements of the PBSE, respectively. ω is the circular frequency. Substituting equation (13) into the first two expressions results in the governing equation in the frequency domain,

$$\begin{cases} -\omega^2 \rho A W(x,\omega) + GA\left(\dfrac{d\Phi(x,\omega)}{dx} - \dfrac{d^2 W(x,\omega)}{dx^2}\right) = 0 \\ -\omega^2 \rho I \Phi(x,\omega) + GA\left(\Phi - \dfrac{dW(x,\omega)}{dx}\right) - EI\dfrac{d^2\Phi(x,\omega)}{dx^2} = 0 \end{cases} \tag{14}$$

Assuming that the general solutions of $W(x,\omega)$ and $\Phi(x,\omega)$ take the forms [52]:

$$\begin{cases} W(x,\omega) = \mathbf{e}(x,\omega)\,\mathbf{B} \\ \Phi(x,\omega) = \mathbf{e}(x,\omega)\,\mathbf{B}_r \end{cases} \tag{15}$$

where

$$\begin{aligned} \boldsymbol{e}(x,\omega) &= \left[e^{\mathrm{i}k_1 x}, e^{\mathrm{i}k_2 x}, e^{-\mathrm{i}k_1 x}, e^{-\mathrm{i}k_2 x}\right] \\ \boldsymbol{B} &= [B_1, B_2, B_3, B_4]^T \\ \boldsymbol{B}_r &= [r_1 B_1, r_2 B_2, -r_1 B_3, -r_2 B_4]^T \end{aligned}.$$

By substituting equation (15) into equation (14), and rearranging the resulting expression in the matrix form and seeking the non-trivial solutions of the coefficient matrix, a characteristic equation is derived, allowing for determining the wavenumber $k_p = \frac{\sqrt{2}}{2}\sqrt{\left(\frac{\rho I}{\rho A}+\frac{EI}{GA}\right)\sqrt{\frac{\omega^2\rho A}{EI}} - (-1)^p\sqrt{\left(\frac{\rho I}{\rho A}+\frac{EI}{GA}\right)^2\frac{\omega^2\rho A}{EI} - 4\frac{\omega^2\rho I}{GA}+4}}$ and coefficient $r_p = \frac{\mathrm{i}\left(k_p^2 - \frac{\omega^2\rho I}{GA}\right)}{k_p}$, where $p = 1$ or 2. The nodal displacement and rotational angle can be calculated by substituting the nodal coordinates into equation (15), as given below:

$$\boldsymbol{d} = \begin{bmatrix} W_1 \\ \Phi_1 \\ W_2 \\ \Phi_2 \end{bmatrix} = \begin{bmatrix} W(0,\omega) \\ \Phi(0,\omega) \\ W(d,\omega) \\ \Phi(d,\omega) \end{bmatrix} = \boldsymbol{H}(\omega)\,\boldsymbol{B} \tag{16}$$

where $\mathbf{H}(\omega)$ is the coefficient matrix.

The shear Q and bending moments M distributed along the Timoshenko beam can be expressed as functions of the spectral components $W(x,\omega)$ and $\Phi(x,\omega)$, respectively, as follows:

$$\begin{cases} Q = GA\left[\frac{\partial W(x,\omega)}{\partial x} - \Phi(x,\omega)\right] \\ M = EI\frac{\partial\Phi(x,\omega)}{\partial x} \end{cases} \tag{17}$$

Note that the voltage induced by the piezoelectric effect generates an additional inherent moment $M_p = \theta V_p$ [53], where V_p is the spectral component of the voltage of the PBSE. Therefore, the total bending moment of the PBSE is given by

$$\widehat{M} = M + M_p = M + \theta V_p. \tag{18}$$

Assuming that the general solutions for the voltage and current in equation (12) are $v_p(t) = V_p e^{\mathrm{i}\omega t}$ and $i_p(t) = I_p e^{\mathrm{i}\omega t}$, respectively, and substituting these into equation (12), the electromechanical coupling equation can be transformed into frequency domain as follows:

$$I_p + \mathrm{i}\omega C_p V_p - \mathrm{i}\omega\theta\left[\Phi(d) - \Phi(0)\right] = 0. \tag{19}$$

Note that the voltage–current relationship is $V_p = I_p Z(\omega)$, where $Z(\omega)$ is the general impedance. Equation (19) can be rewritten as

$$V_p = \frac{\mathrm{i}\omega\theta\left[\Phi(d) - \Phi(0)\right]}{\mathrm{i}\omega C_p + \frac{1}{Z(\omega)}}. \tag{20}$$

When different external circuits are considered, V_p varies, resulting in different $\widehat{M}$ in equation (18). For example, by substituting equation (20) into equation (18) and considering the impedance $Z_c(\omega)$ of the C-F higher-order resonant circuits given in equation (1), the total bending moment $\widehat{M}$ of the PBSE can be calculated as follows

$$\widehat{M} = EI\frac{\partial\Phi(x)}{\partial x} + \frac{\mathrm{i}\omega\theta^2\left[\Phi(d) - \Phi(0)\right]}{\mathrm{i}\omega C_p + \sum_{i=1}^{n}\left(\frac{\mathrm{i}\omega C_i}{1+\mathrm{i}\omega R_i C_i - \omega^2 L_i^* C_i}\right)}. \tag{21}$$

Similar to equation (16), the nodal forces can be obtained by substituting the nodal coordinates to equations (17)

and (21)

$$\boldsymbol{f}=\begin{bmatrix}Q_1\\M_1\\Q_2\\M_2\end{bmatrix}=\begin{bmatrix}-Q(0)\\-\widehat{M}(0)\\Q(d)\\\widehat{M}(d)\end{bmatrix}=\boldsymbol{G}(\omega)\boldsymbol{B}. \tag{22}$$

By relating equations (16) and (22), the relation between the nodal displacement and force can be obtained as

$$\boldsymbol{f}=\boldsymbol{S}(\omega)\boldsymbol{d}=\boldsymbol{G}(\omega)\boldsymbol{H}^{-1}(\omega)\boldsymbol{d} \tag{23}$$

where $\boldsymbol{S}(\omega)$ represents the frequency-dependent dynamics stiffness matrix of the PBSE.

3.3. Spectral transfer matrix method

Band structure, which describes the relation between the circular frequency ω and the wavenumber q, plays an important role in characterizing the wave propagating properties in periodic structures [54]. In this subsection, we employ the STMM to derive the band structure of the piezoelectric metamaterial with arbitrary decoupled defect modes. First, equation (23) is rewritten as:

$$\begin{bmatrix}\boldsymbol{f}_L\\\boldsymbol{f}_R\end{bmatrix}=\underbrace{\begin{bmatrix}\boldsymbol{S}_{LL}&\boldsymbol{S}_{LR}\\\boldsymbol{S}_{RL}&\boldsymbol{S}_{RR}\end{bmatrix}}_{\boldsymbol{S}(\omega)}\begin{bmatrix}\boldsymbol{d}_L\\\boldsymbol{d}_R\end{bmatrix} \tag{24}$$

where the subscripts L and R of $\boldsymbol{f}$ and $\mathbf{d}$ refer to the left and right end nodes of the PBSE, respectively, in which $\boldsymbol{d}_L=[W_L\ \Phi_L]^T$ and $\boldsymbol{d}_R=[W_R\ \Phi_R]^T$. The dynamics stiffness matrix $\boldsymbol{S}(\omega)$ is divided into four 2×2 submatrices. To accurately capture the defect bands, multiple PBSEs, including those with defective configurations, should be assembled end-to-end. The assembled elements are then treated as a new spectral element, referred to as the supercell PBSE. By using the finite element assembly concept, the relation between the nodal forces and displacements of the supercell PBSE can be derived as:

$$\begin{bmatrix}\boldsymbol{f}_L\\\boldsymbol{f}_I\\\boldsymbol{f}_R\end{bmatrix}=\underbrace{\begin{bmatrix}\boldsymbol{S}_{LL}&\boldsymbol{S}_{LI}&\boldsymbol{S}_{LR}\\\boldsymbol{S}_{IL}&\boldsymbol{S}_{II}&\boldsymbol{S}_{IR}\\\boldsymbol{S}_{RL}&\boldsymbol{S}_{RI}&\boldsymbol{S}_{RR}\end{bmatrix}}_{\boldsymbol{S}_S(\omega)}\begin{bmatrix}\boldsymbol{d}_L\\\boldsymbol{d}_I\\\boldsymbol{d}_R\end{bmatrix} \tag{25}$$

where the subscript I denotes the internal nodes of the supercell PBSE. $\boldsymbol{S}_S(\omega)$ denotes the supercell dynamic stiffness matrix, and the dimensions of the submatrices $\boldsymbol{S}_{LI}$, $\boldsymbol{S}_{IL}$, $\boldsymbol{S}_{II}$, and $\boldsymbol{S}_{IR}$ depend on the number of internal nodes. For example, when the supercell PBSE contains two PBSE, there is an internal node that results in the dimension of submatrices being 2×2. Since the dispersion relation calculation considers only applying the Floquet periodic boundary condition at the left and right end nodes of the supercell PBSE, while the internal nodes are unconstrained (i.e. $\boldsymbol{f}_I=0$), one can obtain the supercell condensed dynamic stiffness matrix $\boldsymbol{S}_{SC}(\omega)$:

$$\begin{bmatrix}\boldsymbol{f}_L\\\boldsymbol{f}_R\end{bmatrix}=\underbrace{\begin{bmatrix}\boldsymbol{S}_{LL}-\boldsymbol{S}_{LI}\boldsymbol{S}_{II}^{-1}\boldsymbol{S}_{IL}&\boldsymbol{S}_{LR}-\boldsymbol{S}_{LI}\boldsymbol{S}_{II}^{-1}\boldsymbol{S}_{LR}\\\boldsymbol{S}_{RL}-\boldsymbol{S}_{RI}\boldsymbol{S}_{II}^{-1}\boldsymbol{S}_{IL}&\boldsymbol{S}_{RR}-\boldsymbol{S}_{RI}\boldsymbol{S}_{II}^{-1}\boldsymbol{S}_{IR}\end{bmatrix}}_{\boldsymbol{S}_{sc}(\omega)}\begin{bmatrix}\boldsymbol{d}_L\\\boldsymbol{d}_R\end{bmatrix} \tag{26}$$

in which $\boldsymbol{S}_{SC}(\omega)$ can be rewritten as a matrix consisting of four 2×2 submatrices

$$\boldsymbol{S}_{SC}(\omega)=\begin{bmatrix}\boldsymbol{S}_{LL}^{SC}&\boldsymbol{S}_{LR}^{SC}\\\boldsymbol{S}_{RL}^{SC}&\boldsymbol{S}_{RR}^{SC}\end{bmatrix}. \tag{27}$$

To calculate the band structure, the supercell condensed dynamic stiffness matrix should be converted to a transfer matrix. According to the method in [55], the transfer matrix $\mathbf{T}(\omega)$ can be derived as:

$$\mathbf{T}(\omega)=\begin{bmatrix}-\left(\boldsymbol{S}_{LR}^{SC}\right)^{-1}\boldsymbol{S}_{LL}^{SC}&-\left(\boldsymbol{S}_{LR}^{SC}\right)^{-1}\\\boldsymbol{S}_{RL}^{SC}-\boldsymbol{S}_{RR}^{SC}\left(\boldsymbol{S}_{LR}^{SC}\right)^{-1}\boldsymbol{S}_{LL}^{SC}&-\boldsymbol{S}_{RR}^{SC}\left(\boldsymbol{S}_{LR}^{SC}\right)^{-1}\end{bmatrix}. \tag{28}$$

The transfer matrix $\mathbf{T}(\omega)$ describes the dynamics of the left and right nodes of a beam element in the form of $\boldsymbol{u}_R=\mathbf{T}(\omega)\boldsymbol{u}_L$, where $\boldsymbol{u}_L^T=\begin{bmatrix}\boldsymbol{d}_L&\boldsymbol{f}_L\end{bmatrix}^T$, and $\boldsymbol{u}_R^T=\begin{bmatrix}\boldsymbol{d}_R&\boldsymbol{f}_R\end{bmatrix}^T$. The band structure, i.e. the diagram of wavenumber q versus ω, can be calculated by solving the expression [56]:

$$\left|\mathbf{T}(\omega)-e^{\mathrm{i}qd}\boldsymbol{I}\right|=0 \tag{29}$$

where $\boldsymbol{I}$ is the unit matrix. Note that the relation between the real part of q and ω describes the propagating wave and the range of ω values that yield no real solutions for q corresponds to the bandgap.

In addition, to investigate the dynamics behavior of the defective piezoelectric metamaterial with finite unit cells, the harmonic response of the proposed metamaterial beam at the center point (along the x-axis) is calculated under clamped-clamped boundary conditions, which are more suitable for demonstration of the vibration energy localization effect. To be specific, the left and right end of the piezoelectric metamaterial beam is subjected to a 1 N force, while the rotation displacement of these two ends is constrained to zero. The harmonic response τ of the defective piezoelectric metamaterial beam at the center point is defined as

$$\tau=20\log_{10}\left(\left|W(kd/2,\omega)/W(0,\omega)\right|\right) \tag{30}$$

where $W(0,\omega)$ is the transverse displacement at the left end, determined by applying the clamped-clamped boundary conditions to equation (25) and subsequently solving the corresponding matrix equation. $W(kd/2,\omega)$ is the transverse displacement at the center point of the metamaterial beam, obtained by substituting the coefficients from the previous step into equation (15).

4. Multi-bandgap decoupling tuning method

This section focuses on presenting a multi-bandgap decoupling tuning method based on C-F higher-order resonant circuits, which provides a foundation for generating multiple defect modes with independent tunability. To facilitate comparison and highlight the advantages of the proposed method, we first introduce a conventional higher-order resonant circuit.

The diagram of a conventional high-order resonant circuit [46] used for generating multiple bandgaps in a piezoelectric metamaterial is shown in figure 4(a). The resistor-inductor-capacitor loops R_i-L_i-C_i, $i = 2, 3, \ldots, n$, (orange part in figure 4(a)) increase the DOF of the electromechanical resonator, contributing to additional bandgaps. For this higher-order resonant circuit, the total shunt branches impedance $Z_j^h(s)$ with n R_i-L_i-C_i loops in the jth unit cell can be expressed by Laplace form as:

$$Z_j^h(s) = \cfrac{1}{\cfrac{1}{\cfrac{1}{\cfrac{1}{\vdots\left\{\cfrac{1}{\cfrac{1}{sL_{n-1}+R_{n-1}+\cfrac{sL_n+R_n}{1+sC_nR_n+s^2L_nC_n}}+sC_{n-1}}+R_{n-2}+sL_{n-2}}\ddots\right.}+sC_3}+R_2+sL_2}+sC_2}+R_1+sL_1 \tag{31}$$

As shown in figure 4(b), this conventional higher-order resonant circuit can be equivalently represented as a multi-DOF vibration absorber using the electrical-mechanical analogy. Subsequently, we will derive the bandgap tuning expressions for both circuit configurations shown in figures 2(c) and 4(a), respectively.

Based on the theory of negative bending stiffness, the analytical expressions of bandgap bounds can be derived. Specifically, when the effective bending stiffness D_{eff} of the piezoelectric-beam element, as given below, becomes negative at a certain frequency, bandgaps emerge in piezoelectric metamaterials [57].

$$D_{\text{eff}} = E_s I_s + E_p^{\text{eff}} I_{ps} \tag{32}$$

where $I_{ps} = b\left[(h_s+2h_p)^3 - {h_s}^3\right]\Big/12$. $E_p^{\text{eff}} = E_p^{\text{oc}}\left[1 - k_{31}^2/\left(1+sC_pZ_j(s)\right)\right]$ are the effective Young's modulus of piezoelectric layers, where $E_p^{\text{oc}} = 1/\left(S_{11}^{\text{E}} - S_{11}^{\text{E}}k_{31}^2\right)$ is the open-circuit condition Young's modulus. $k_{31} = \sqrt{d_{31}^2/\left(S_{11}^{\text{E}}\varepsilon_{33}^{\text{T}}\right)}$ is the electromechanical coupling coefficient. In other words, bandgap bounds can be determined by solving $D_{\text{eff}} = 0$, where the upper bounds of the bandgaps are solely dependent on the characteristic roots of $1 + sC_pZ_j(s) = 0$. For the sake of presentation, consider $n = 2$ (i.e. two bandgaps are expected to create) and omit the resistance R, thereby the impedance of the C-F higher-order resonant circuit (i.e. the one shown in figure 2(c)) can be simplified as:

$$Z_j^c(s) = \frac{1}{\frac{sC_1}{1+s^2L_1^*C_1} + \frac{sC_2}{1+s^2L_2^*C_2}} \tag{33}$$

in which $L_i^* = \frac{C_p+C_i}{\bar{\Omega}_i^2 C_pC_i}$, for $i = 1, 2$, where $\bar{\Omega}_i$ is the desired resonant frequency. Substituting equation (33) into $1 + sC_pZ_j(s) = 0$ and solving for its characteristic roots, one can obtain the analytical expressions for the upper bounds of bandgaps.

$$\text{BG}_{1,\text{up}} = \sqrt{\frac{A_1 - \sqrt{A_2A_3} + A_4}{2A_2}} \tag{34}$$

$$\text{BG}_{2,\text{up}} = \sqrt{\frac{A_1 + \sqrt{A_2A_3} + A_4}{2A_2}} \tag{35}$$

where $\text{BG}_{1,\text{up}}$ and $\text{BG}_{2,\text{up}}$ denote the upper bounds of the bandgap at lower and higher frequencies, and

$$\begin{aligned}
A_1 &= \left(\bar{\Omega}_1^2 + \bar{\Omega}_2^2\right)(C_1C_2 + C_1C_p + C_2C_p)\\
A_2 &= (C_1 + C_p)(C_2 + C_p)\\
A_3 &= \left(\bar{\Omega}_1^4 + \bar{\Omega}_2^4\right)(C_1C_2 + C_1C_p + C_2C_p) - 2\bar{\Omega}_1^2\bar{\Omega}_2^2(C_1C_p\\
&\quad -C_1C_2 + C_2C_p) + C_p^2\left(\bar{\Omega}_1 + \bar{\Omega}_2\right)^2\left(\bar{\Omega}_1 - \bar{\Omega}_2\right)^2\\
A_4 &= C_p^2\left(\bar{\Omega}_1^2 + \bar{\Omega}_2^2\right).
\end{aligned}$$

Assuming that capacitances C_1 in the C-F higher-order resonant circuit tends to zero, equations (34) and (35) can be further simplified by considering the limiting values $\lim_{C_1\to 0} A_1 = C_2C_p\left(\bar{\Omega}_1^2 + \bar{\Omega}_2^2\right)$, $\lim_{C_1\to 0} A_2 = C_p(C_2 + C_p)$, and $\lim_{C_1\to 0} A_3 = C_2C_p\left(\bar{\Omega}_1^2 - \bar{\Omega}_2^2\right)^2 + C_p^2\left(\bar{\Omega}_1 + \bar{\Omega}_2\right)^2\left(\bar{\Omega}_1 - \bar{\Omega}_2\right)^2$ to yield:

$$\text{BG}_{1,\text{up}} = \bar{\Omega}_1, \textit{ for } C_1 \to 0 \tag{36}$$

$$\text{BG}_{2,\text{up}} = \bar{\Omega}_2, \text{ for } C_1 \to 0. \tag{37}$$

Similarly, as C_2 approaches zero, the following relationship is obtained:

$$\text{BG}_{1,\text{up}} = \bar{\Omega}_1, \textit{ for } C_2 \to 0 \tag{38}$$

$$\text{BG}_{2,\text{up}} = \bar{\Omega}_2, \text{ for } C_2 \to 0. \tag{39}$$

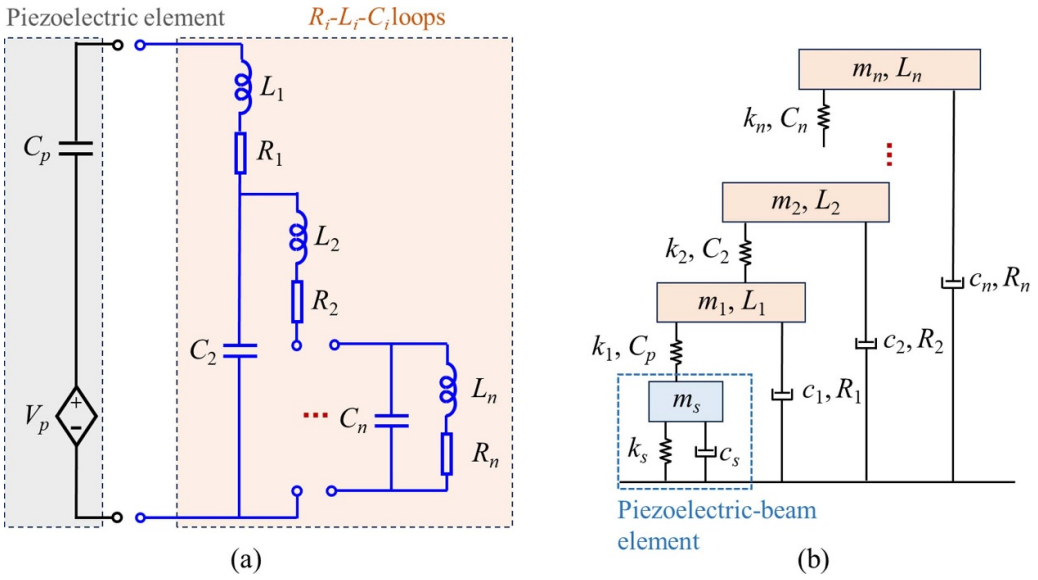

Figure 4. (a) The diagram of the higher-order resonant circuit with R_i-L_i-C_i loops used in [46]; (b) The equivalent mechanical model of the higher-order resonant circuit based on electrical-mechanical analogy. Reproduced from [46]. © IOP Publishing Ltd All rights reserved.

Equations (34)–(39) define the multi-bandgap decoupled tuning method, which demonstrated that, provided the capacitances of the circuit satisfy near-zero regulation, the bandgaps are decoupled and can be independently tuned to any desired resonance frequency (e.g. $\bar{\Omega}_1$ and $\bar{\Omega}_2$). This method also makes it possible to obtain arbitrary decoupled defect modes. It should be pointed out that the lower bound of the bandgaps can also be determined by solving $D_{\text{eff}} = 0$. Due to the excessive length of the resulting expression, it has been omitted from this paper.

For comparison, we examine the bandgap tuning properties based on the conventional higher-order resonant circuit (i.e. the one shown in figure 4(a)), whose impedance at $n = 2$ can be rewritten as:

$$Z_j^h(s) = sL_1 + \frac{sL_2}{1 + s^2 L_2 C_2} \tag{40}$$

with the same procedure, the upper bounds of bandgaps can be derived as:

$$\text{BG}_{1,\text{up}} = \frac{\sqrt{\frac{1}{2}\left((\Omega_1\Omega_2)^2 + (\Omega_1\Omega_3)^2 + (\Omega_2\Omega_3)^2 + \sqrt{\left(\Omega_2^2 + \Omega_3^2\right)^2\Omega_1^4 + 2(\Omega_1\Omega_2\Omega_3)^2\left(\Omega_2^2 - \Omega_3^2\right) + (\Omega_2\Omega_3)^4}\right)}}{\Omega_3} \tag{41}$$

$$\text{BG}_{2,\text{up}} = \frac{\sqrt{\frac{1}{2}\left((\Omega_1\Omega_2)^2 + (\Omega_1\Omega_3)^2 + (\Omega_2\Omega_3)^2 + \sqrt{\left(\Omega_2^2 + \Omega_3^2\right)^2\Omega_1^4 + 2(\Omega_1\Omega_2\Omega_3)^2\left(\Omega_2^2 - \Omega_3^2\right) + (\Omega_2\Omega_3)^4}\right)}}{\Omega_3} \tag{42}$$

where $\Omega_1 = 1/\sqrt{L_1 C_p}$, $\Omega_2 = 1/\sqrt{L_2 C_2}$, and $\Omega_3 = 1/\sqrt{L_2 C_p}$. It can be noticed that changing any of the resonant frequencies Ω_1, Ω_2, and Ω_3 simultaneously adjusts the frequency bands of both bandgaps, implying that the defect bands formed in these bandgaps are also frequency-shifted. In addition, it is to be expected that as the resonance order increases, the closed-loop tuning solution will become more complex and will require readjustment of circuit parameters to keep the previously created bandgaps unchanged.

Furthermore, as shown in equations (36)–(39), the decoupling tuning characteristics of the multiple bandgaps depend on the capacitance values in the C-F higher-order resonant circuit. A numerical example is given to analyze the impact of capacitance C_1 and C_2 in equation (33) on the bandgaps. Letting $\bar{\Omega}_1 = 200$ and $\bar{\Omega}_2 = 300$ Hz. The evolution of first and second bandgaps, i.e. BG1 and BG2, as C_1 and C_2 vary is illustrated in figures 5(a) and (b), respectively. The red and blue surfaces denote the upper and lower bounds of BG1 and BG2, while the black dash lines are the reference for $\bar{\Omega}_1 = 200$ Hz and $\bar{\Omega}_2 = 300$ Hz. It can be seen that as either C_1 or C_2 approaches zero, the upper bounds of BG1 and BG2 align with their respective desired resonant frequencies, $\bar{\Omega}_1$ and $\bar{\Omega}_2$, thus confirming the validity of equations (36)–(39). Meanwhile, it is observed that when both C_1 and C_2 approach zero, it

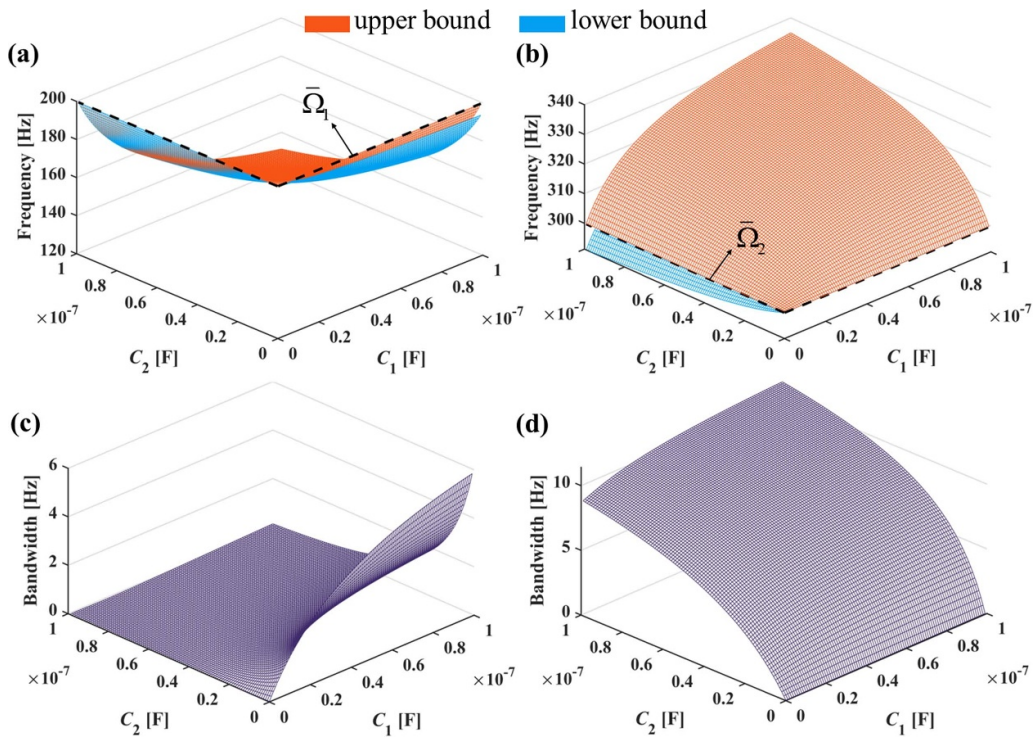

Figure 5. Variation in bandgap bounds of the piezoelectric metamaterial shunted with C-F higher-order resonant circuits as C1 and C2 vary: (a) BG1 and (b) BG2; variation in the bandwidths of bandgaps as C1 and C2 vary: (c) BG1 and (d) BG2.

results in the closure of the two bandgaps. For further details, figures 5(c) and (d) depict the variation in the bandwidths of BG1 and BG2, defined as the width between the upper and lower bounds, for different C_1 and C_2. For BG1, an increase in C_1 contributes to bandwidth expansion, whereas an increase in C_2 results in bandwidth reduction. In contrast, the bandwidth of BG2 broadens as C_1 and C_2 increase, with this trend being more pronounced as C_2 increases. Therefore, to ensure that the bandwidths of BG1 and BG2 are comparable, while minimizing the interference between the tuning of the two bandgaps, it is recommended to use a smaller C_2 to satisfy equations (38) and (39). Based on the above analysis, $C_1 = 100$ and $C_2 = 1$ nF will be used for the C-F higher-order resonant circuit at $n = 2$.

5. Results and discussion

This section commences with verification and discussion of the piezoelectric metamaterial beam with a single defect band through spectral and harmonic response analysis. Later, the properties of arbitrary decoupled defect modes are examined in detail.

5.1. Piezoelectric metamaterial with a single defect band

In this subsection, the defect mode properties of the piezoelectric metamaterial when all cells are shunted with the first-order resonant circuits shown are discussed. In this setup, the inductance of the defective cells is intentionally adjusted differently from that of the non-defective cells to create a single defect band. This subsection provides a comprehensive analysis of how the wave localization behavior of the defect mode is influenced by factors such as open and short circuits at the defective cell, the defect-mode frequency, and the electro-damping induced by resistance. It also highlights the limitations of the single defect band, setting the stage for exploring arbitrary decoupled defect modes in section 5.2.

First, the band structures of a piezoelectric metamaterial beam shunted with first-order resonant circuits, both without and with a piezoelectric defect, are computed based on the STMM established in section 3.3. The first-order resonant circuit (i.e. the one shown in figure 2(a)) consists solely of an inductor with an inductance of 8.48 H, corresponding to an LC resonant frequency of $\Omega = 250$ Hz. The resistance R is not considered in any of the band structure analyses in this paper, as the bandgap is, by definition, undamped. The effect of R on the dynamic response will be discussed later. The supercell PBSE consists of 5 unit cells (i.e. $k = 5$). The material/geometric parameters are given in table 1. Figure 6(a) shows the band structure of the piezoelectric metamaterial supercell without defect. RE(q^*) denotes the real part of the dimensionless wavenumber $q^* = qkd/\pi$. The black solid curve presents solutions calculated using the STMM, while the red points represent results from COMSOL. Figure 6(a) illustrates that the spectral analysis results closely match those from COMSOL. Additionally, the band structure for a single-cell is superimposed in figure 6(a). It is important to note that the number of propagating bands in the supercell results is greater

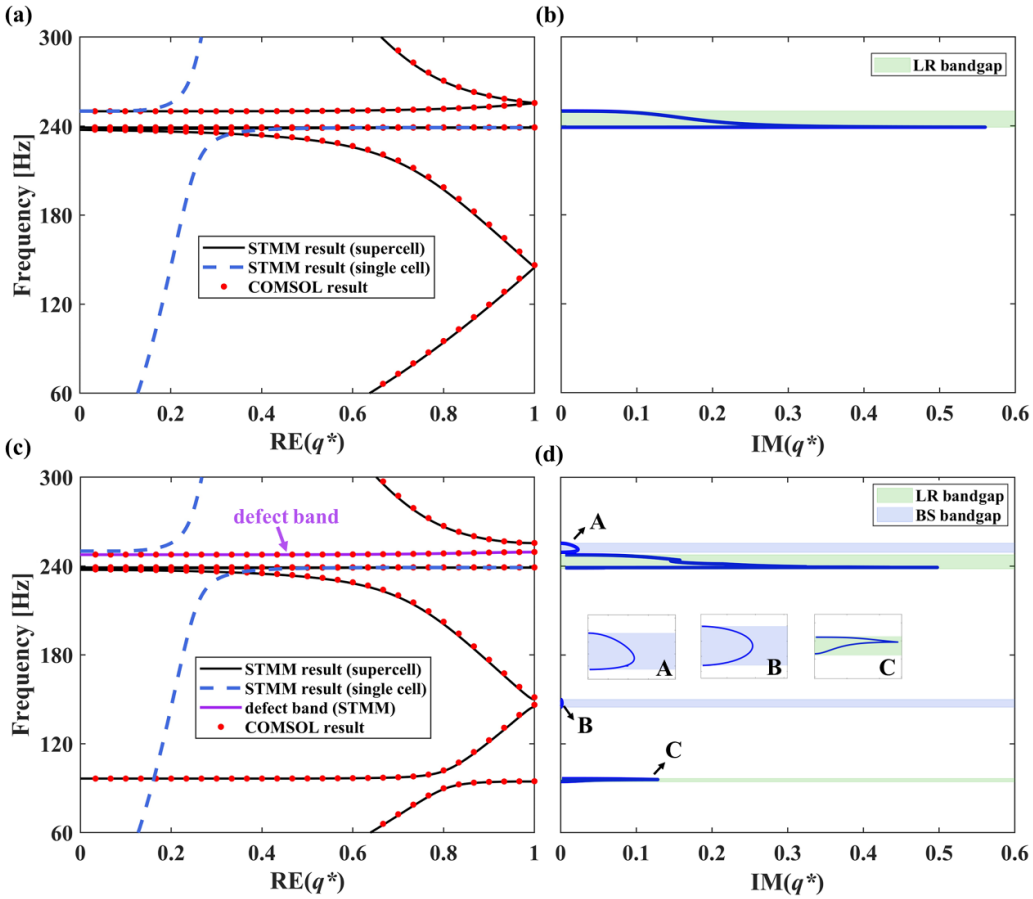

Figure 6. The band structure of the piezoelectric metamaterial without defect: (a) the real part and (b) the imaginary part of the dimensionless wavenumber; the band structure of the piezoelectric metamaterial with a single defect band: (c) the real part and (d) the imaginary part of the dimensionless wavenumber. The black solid curve and red point are STMM and COMSOL results, respectively, under the supercell configuration. The blue dashed curve is STMM result under the single-cell configuration. The defect band is indicated by a pink solid curve.

than that in the single-cell result, due to band folding in the reduced supercell Brillouin zone [58]. In contrast, the bandgap frequency range remains constant. Figure 6(b). Shows the imaginary part of the dimensionless wavenumber, i.e. IM (q^*), versus frequency. A sharp spike can be seen within the bandgap formed from 239.1 to 249.99 Hz (shaded in green), implying that this bandgap should be the LR mechanism-induced bandgap. Besides, the values of IM (q^*) represent the strength of wave attenuation, the larger Imag (q^*) is, the stronger the wave attenuation effect of the bandgap.

Next, the defective cell is constructed by intentionally setting the inductance assigned to the center cell (i.e. the third cell) to 53 H, resulting in an LC resonance frequency of the defective cell of $\Omega_d = 100$ Hz. Figure 6(c) displays the band structure of the piezoelectric metamaterial with the defective cell. A defect band, i.e. the pink solid curve, appears from 247.7 to 249.4 Hz. According to the theory of defective metamaterial, the evanescent wave will be confined inside and in the vicinity of the defective cell, which is known as wave localization. The underlying mechanism of wave localization is attributed to the nearly zero energy transport velocity of the wave at defect modes, as evidenced by the almost zero slope of the defect band. In addition, figure 6(d) shows the imaginary part evolution of the dimensionless wavenumber of the piezoelectric metamaterial supercell. Similar to figure 6(b), an LR bandgap emerges from 238.3 to 247.7 Hz, which is shaded in green. Besides, an additional LR bandgap is created around Ω_d, which is induced by the circuitry resonance related to the defective cell. It is worth noting that three unexpected BS bandgaps (shaded in blue) appear at the folding points of the band structure, with a smoother evolution of the imaginary part of q^*, as shown in the subfigures A and B in figure 6(d). This phenomenon is due to the combined effect of band folding and aperiodicity introduced by the defective cell, which was also reported in detail in [51]. Moreover, the defect band can be found between the LR and BS bandgaps, which is consistent with other findings that defect mode always forms within the bandgap.

Subsequently, the harmonic responses τ of piezoelectric metamaterial beams, consisting of 11 unit cells with a point defect located at the center (i.e. the 6th cell), are calculated using the SEM, as illustrated in figure 7(b). The materials and geometric parameters listed in table 1 are used. The resonant frequencies $\Omega_d = 100$ and $\Omega = 250$ Hz are assigned to the defective and defect-free cells, respectively. As a comparison, figure 7(a) illustrates the harmonic response of

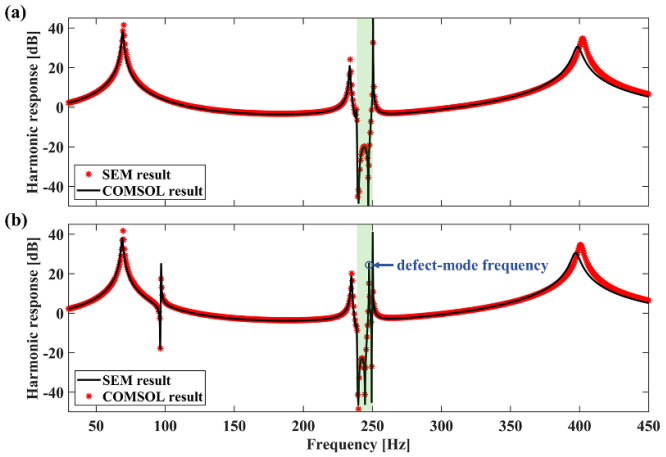

Figure 7. The harmonic response of the piezoelectric metamaterial beams consisting of 11 unit cells: (a) without defect; and (b) with a point defect. The black solid curve and red asterisk are SEM and COMSOL results, respectively. The defect-free bandgap range is shaded in green. A defect-mode frequency related to the defect mode is indicated in figure (b).

the piezoelectric metamaterial beam without defect. For this dynamic response, the resistance $R = 50$ [Ω] is included in the first-order resonant circuit for all cells (the unit of resistance, [Ω], is to distinguish it from the resonant frequency symbol Ω). The range of LR bandgap observed in figure 6(b) is highlighted in green in figure 7. It is seen that SEM results are in good agreement with the COMSOL simulations. Notably, a defect mode, identified by the peak frequency in figure 7(b), appears within the bandgap due to the piezoelectric defect. This peak frequency is defined as the defect-mode frequency Ω_{defect}.

To gain insight into the defect mode, figures 8(a) and (b) show the contours of the normalized wave mode shape, represented by $|W(x, \omega)/\max(W(x, \omega))|$, as a function of frequency for both defect-free and defective piezoelectric metamaterial beams. The x-axis denotes the normalized length of the beam. The white and blue colors mean weak and intense vibrations, respectively. A visible LR bandgap can be seen in figure 8(a). As a comparison, figure 8(b) illustrates a pronounced vibration at the center of the piezoelectric metamaterial beam within the bandgap, exactly around the defect-mode frequency Ω_{defect}. This is attributed to the wave localization effect.

Subsequently, the defect mode properties are explored by fixing $\Omega = 250$ Hz, and varying the Ω_{d} of the defective cell. Figure 9(a) shows the evolution of Ω_{defect} as Ω_{d}/Ω varies. When $\Omega_{\text{d}}/\Omega < 1$, Ω_{defect} decreases with a reduction in Ω_{d}, starting near the upper bound of the defect-free bandgap and trending towards 247.6 Hz (i.e. the case of A). Conversely, for $\Omega_{\text{d}}/\Omega > 1$, Ω_{defect} increases from near the lower bound of the defect-free bandgap, rising to 247.3 Hz (i.e. the case of D) as Ω_{d} increases. Note that when $\Omega_{\text{d}}/\Omega = 1$, the piezoelectric metamaterial with a defect degenerates into a uniform metamaterial and thus has no defect mode. In addition, the values of Ω_{defect} corresponding to $\Omega_{\text{d}} \to 0$ and $\Omega_{\text{d}} \to \infty$ are governed by the stiffness of the piezoelectric element in the open-circuit and short-circuit conditions, respectively. This is because, to achieve Ω_{d} approaching zero or infinity, the impedance of the shunt circuit must be adjusted to infinity or zero, respectively. According to equation (32), the equivalent Young's modulus of the piezoelectric element converges to E_p^{oc} and $E_p^{\text{oc}}\left(1 - k_{31}^2\right)$ under open-circuit and short-circuit conditions, respectively. To investigate the differences in the wave localization effects of defect modes with varying Ω_{d}/Ω, the normalized wave mode shapes related to four cases of Ω_{defect} (i.e, A-D) are presented in figures 9(b) and (c) shows the contours of wave mode shapes at the corresponding Ω_{defect}. It can be found that when Ω_{d}/Ω deviates significantly from 1, the wave localization effect intensifies. In other words, the vibration energy concentrates near the defective cells, while vibrations in other regions are suppressed. On the contrary, when Ω_{d}/Ω closes to 1, it is seen that the wave localization effect diminishes.

To further explore the properties of the defect mode under varying resonance frequency Ω, figure 10 shows the contours of the normalized wave mode shapes of the defective piezoelectric metamaterial at its defect-mode frequency Ω_{defect} for $\Omega = 250$, 350, 450, 600, 750, and 900 Hz. Two cases are examined: $\Omega_{\text{d}} = 1$ and $\Omega_{\text{d}} = 5000$ Hz, corresponding to the cases of $\Omega_{\text{d}}/\Omega < 1$ and $\Omega_{\text{d}}/\Omega > 1$, as illustrated in figures 10(a) and (b), respectively. Ω_{defect} obtained at the above resonant frequencies Ω have been given in figure 10. The results indicate that wave localization weakens with increasing Ω, as evidenced by the vibration energy no longer being confined to the defective cell of the piezoelectric metamaterial, which is particularly pronounced when $\Omega > 600$ Hz. In other words, the energy-localized behavior of defect mode created through piezoelectric resonance exhibits a frequency dependence, a feature not previously discussed in other literature. In addition, the tendency for wave localization to weaken is more evident when $\Omega_{\text{d}}/\Omega > 1$ than when $\Omega_{\text{d}}/\Omega < 1$.

Furthermore, we investigate the effect of the resistance connected in each cell on the energy-localized behavior of the defective piezoelectric metamaterial. Figure 11(a) shows the harmonic response as the resistance R varies, with the $\Omega = 250$ and $\Omega_{\text{d}} = 1$ Hz. As R increases, the trough value of the bandgap region (green shaded area) increases, while the peak of the defect-mode frequency decreases, implying that both the wave attenuation and localization effects are weakened. This phenomenon is due to the electro-damping induced by the resistance, which diminishes the electrical resonance effect. Notably, when $R = 1600$ [Ω], both the bandgap and defect mode vanish. To illustrate above findings more clearly, figure 11(b) presents the normalized wave mode shapes corresponding to the different cases of R shown in figure 11(a), demonstrating how the wave localization strength decreases with increasing electro-damping. Above results highlight the necessity of minimizing parasitic resistance in practical circuit design. Note that traditional inductive circuit implementations typically rely on synthetic circuits composed of analog electronic components [59, 60]. However, due to the non-ideal characteristics of operational amplifiers (op-amps), which introduce biased currents and voltages, parasitic

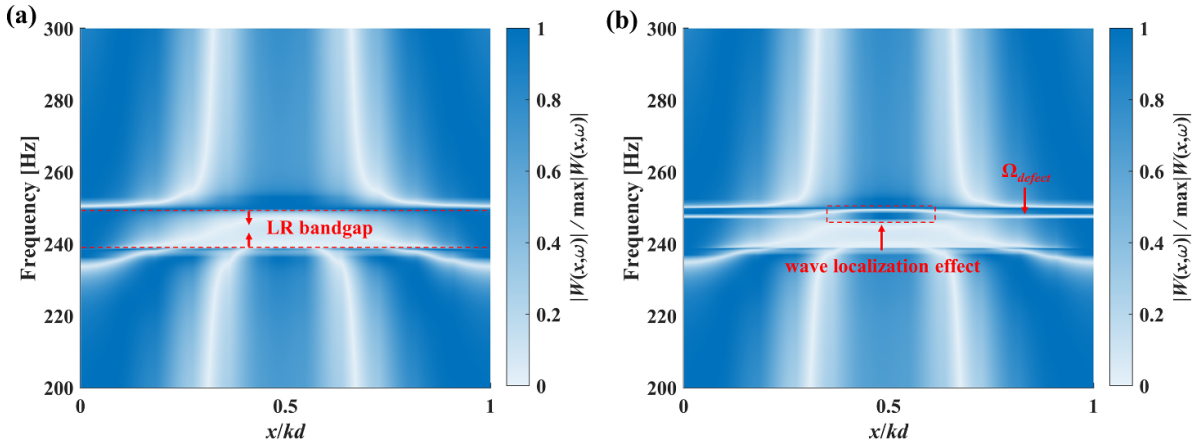

Figure 8. Contours of the normalized wave mode shape as a function of frequency for piezoelectric metamaterial beams: (a) without defect; and (b) with a point defect. The white and blue colors indicate weak and intense vibrations, respectively.

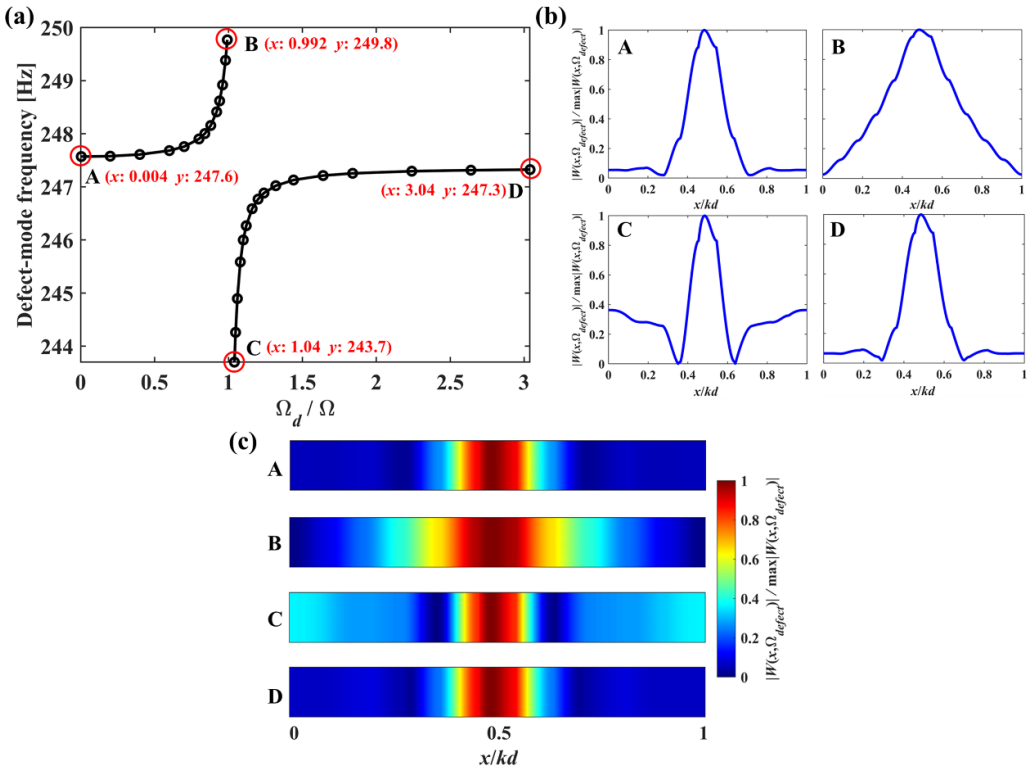

Figure 9. (a) The evolution of the defect-mode frequency Ω_{defect} with varying Ω_{d}/Ω. The four limiting values of Ω_{defect} (i.e. A-D), along with their corresponding coordinates on the *x*-axis and *y*-axis are explicitly labeled in the figure; (b) the normalized wave mode shapes correspond to four cases of Ω_{defect} A-D in (a); (c) Contours of normalized wave mode shapes at the corresponding Ω_{defect}.

resistances are unavoidable [61]. To overcome this issue, it is recommended to use programmable digital circuits [62–64] for implementing the higher-order resonant circuits presented in this paper for practical applications. Programmable digital circuits can simulate the voltage–current relationships of real circuits by programming transfer functions, enabling nearly zero-resistance electrical resonance [64].

Based on the findings of this subsection, the resistance of all loops in the circuit will be fixed at $R = 50$ [Ω] in subsequent analyses. In addition, the case where $\Omega_{\text{d}}/\Omega < 1$, with $\Omega < 750$ Hz, is considered, selecting values of Ω_{d}/Ω significantly different from 1 to enhance the defect mode formation.

5.2. Piezoelectric metamaterial with arbitrary decoupled defect modes

This subsection investigates the characteristics of decouplable broadband defect bands in defective piezoelectric metamaterials for the design introduced in section 2. Apart from the circuit configuration, the material and geometrical parameters are

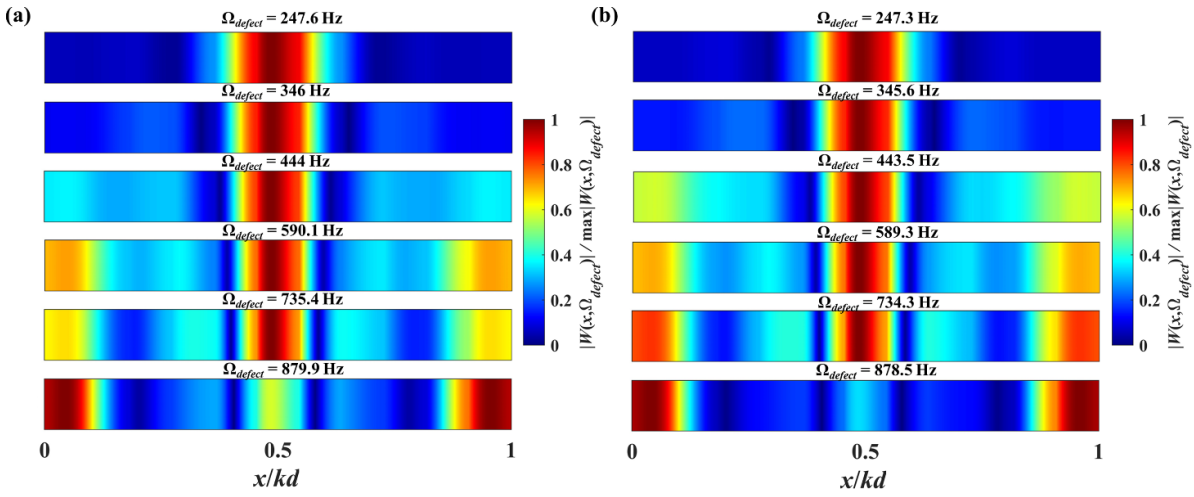

Figure 10. Contours of the normalized wave mode shapes of the defective piezoelectric metamaterial at its defect-mode frequency Ω_{defect} for different Ω in the cases of (a) $\Omega_{\text{d}} = 1$ Hz; and (b) $\Omega_{\text{d}} = 5000$ Hz. Ω_{defect} obtained for $\Omega = 250$, 350, 450, 600, 750, and 900 Hz are presented.

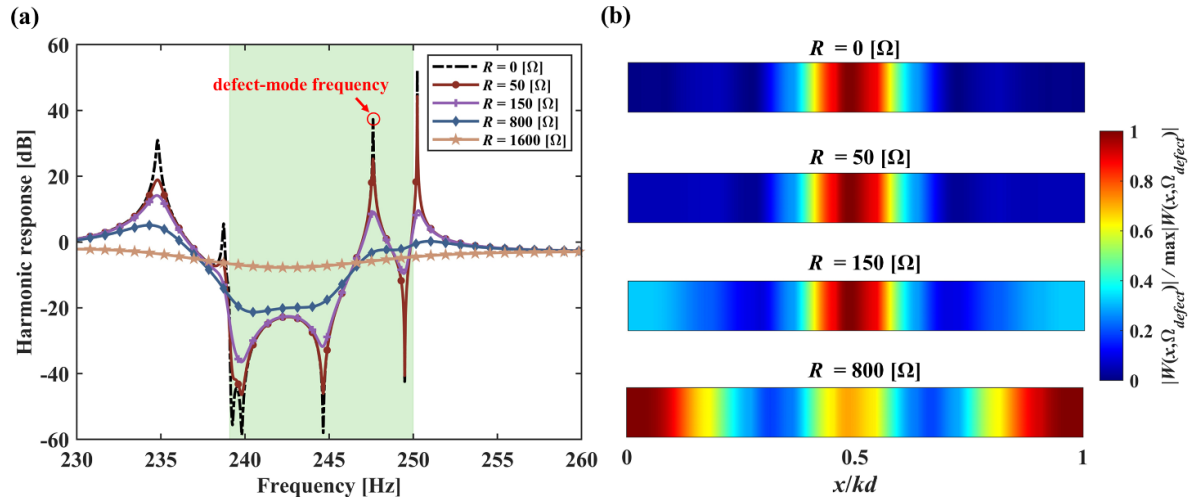

Figure 11. (a) The harmonic response of the defective piezoelectric metamaterial beams for different resistance R in the cases of $\Omega = 250$ and $\Omega_d = 1$ Hz; (b) Contours of the normalized wave mode shapes of the defective piezoelectric metamaterial at its defect-mode frequency Ω_{defect} for different R.

consistent with those in section 5.1. For analytical simplicity, the C-F higher-order resonant circuit is initially configured as second-order ($n = 2$), resulting in two LR bandgaps. Based on the preceding analysis, to achieve a pronounced wave localization effect, the desired resonant frequencies $\bar{\Omega}_1$ and $\bar{\Omega}_2$ of the C-F higher-order resonant circuit in non-defective cells are constrained within 750 Hz, while the desired resonance frequency in the defective cell is set to $\bar{\Omega}_d = 1$ Hz. Additionally, as discussed in section 4, the capacitances $C_1 = 100$ and $C_2 = 1$ nF in the C-F higher-order resonant circuit are used to ensure that the two LR bandgaps have comparable widths.

Considering the supercell PBSE configuration, figures 12(a) and (b) illustrate the band structure of the defect-free piezoelectric metamaterial shunted with C-F higher-order resonant circuits. The desired resonant frequencies in the shunt circuit are set to $\bar{\Omega}_1 = 200$ and $\bar{\Omega}_2 = 300$ Hz. The real part of the dimensionless wavenumber obtained from the single-cell configuration is also depicted in figure 12(a). One can find that the STMM results for the supercell piezoelectric metamaterial highly match the COMOSL results. In addition, two LR bandgaps, denoted as BG1 and BG2, are observed around $\bar{\Omega}_1$ and $\bar{\Omega}_2$, which is attributed to LC resonance.

Note that BG1 and BG2 are relatively narrow, depending on the values of circuit parameters C_1 and C_2. As detailed in section 4, there is a trade-off between expanding the bandwidth of bandgaps and ensuring that multiple bandgaps can be independently tuned. However, this trade-off does not impact the formation of defect modes. Due to the near-zero energy transport velocity characteristic of defect bands, they retain narrowband properties even when situated within a broader bandgap. Consequently, the most effective method for broadening the operational frequency range of defect modes is to create multiple defect bands. Figures 12(c) and (d) present the band structure of the defective piezoelectric metamaterial

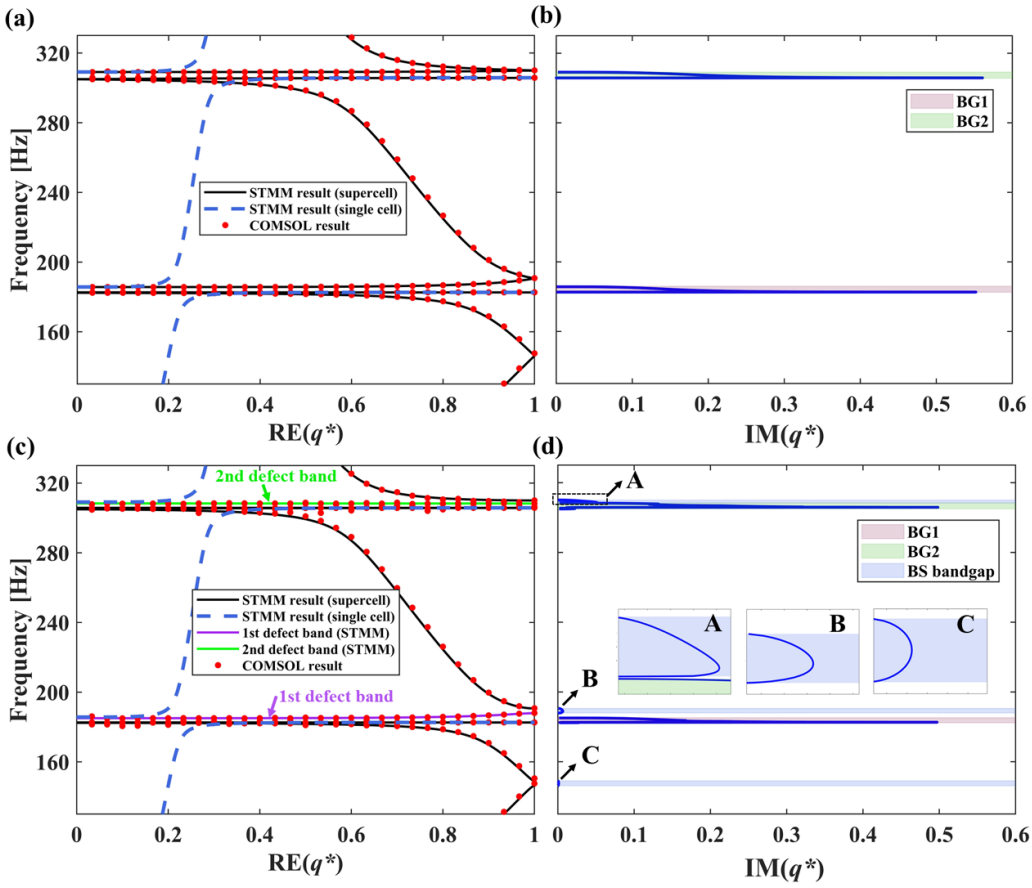

Figure 12. The band structure of the defect-free piezoelectric metamaterial shunted with C-F higher-order resonant circuit: (a) the real part and (b) the imaginary part of the dimensionless wavenumber; The band structure of the defective piezoelectric metamaterial shunted with C-F higher-order resonant circuit: (c) the real part and (d) the imaginary part of the dimensionless wavenumber. The black solid curve and red point are STMM and COMSOL results, respectively, under the supercell configuration. The blue dashed curve is STMM result under the single-cell configuration. The defect bands close to BG1 and BG2, referred to as the 1st defect band and 2nd defect band, are indicated by a pink and green solid curve, respectively.

shunted with C-F higher-order resonant circuits. Similar to the findings in figure 6(c), new BS bandgaps are formed at the folding points RE ($q^* = 1$). The passbands between these BS bandgaps and LR bandgaps are identified as defect bands, referred to as the 1st defect band and 2nd defect band, based on their proximity to BG1 or BG2.

Subsequently, the independent tunability of the two defect bands is verified by examining the frequency variations of the two defect bands when $\bar{\Omega}_1$ is fixed at 200 Hz and $\bar{\Omega}_2$ varied. Figures 13(a)–(f) shows the band structure of the defective piezoelectric metamaterial incorporating C-F higher-order resonant circuit, as calculated using the STMM for the cases of $\bar{\Omega}_2 = 225$, 300, 375, 450, 525, and 600 Hz, respectively. From the results shown in figures 13(b)–(f), one can observe that as $\bar{\Omega}_2$ changes, the frequency of the 2nd defect band can consistently be tuned to the vicinity of $\bar{\Omega}_2$, whereas the frequency of the 1st defect band remains largely unaffected. In particular, figure 13(g) illustrates the case where the inductance in the 2nd loop of the circuit is perturbed and becomes non-functional (i.e. $L_2^* = 0$in equation (33)). It can be seen that, due to the elimination of the resonance function of the 2nd loop, both the 2nd defect band and the bandgap disappears, while the 1st defect band is not affected. These findings confirm that the frequencies of the two defect bands can be independently adjusted by tuning the desired resonance frequency $\bar{\Omega}_1$ and $\bar{\Omega}_2$.

However, as shown in figure 13(a), when $\bar{\Omega}_1$ and $\bar{\Omega}_2$are relatively close, the 2nd defect band shifts toward lower frequencies. To explore this further, figure 14 presents the frequencies of the 1st and 2nd defect bands, obtained through band structure analysis with a fixed $\bar{\Omega}_1$ of 200 Hz, while varying $\bar{\Omega}_2$ from 210 to 600 Hz. The defect band frequencies are taken at RE (q^*) = 0 in the band structure. It is observed that as $\bar{\Omega}_2$ approaches $\bar{\Omega}_1$, the frequency of the 1st defect band decreases, with this trend becomes more pronounced as the resonant frequencies become closer. The zoomed-in view of figure 14 clearly shows this phenomenon. These results indicate that the frequency adjustment of multiple defect modes is no longer completely independent.

The issue arises from the choice of capacitances, $C_1 = 100$ and $C_2 = 1$ nF, to balance the bandgap width, which results in non-ideal switching characteristics of the current branches in the C-F higher-order resonant circuit. Consequently, when the resonant frequencies are far apart, one loop resonates while the other loops can effectively treated as open circuits. However,

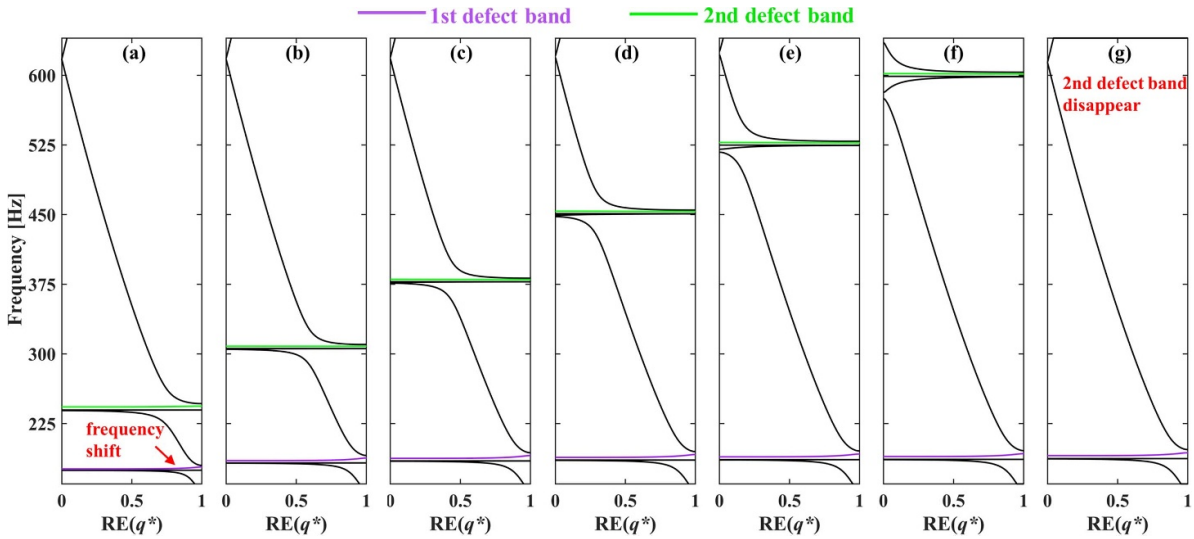

Figure 13. The evolution of the two defect bands in the defective piezoelectric metamaterial incorporating C-F higher-order resonant circuit under the condition where $\bar{\Omega}_1 = 200$ Hz and: (a) $\bar{\Omega}_2 = 225$ Hz; (b) $\bar{\Omega}_2 = 300$ Hz; (c) $\bar{\Omega}_2 = 375$ Hz; (d) $\bar{\Omega}_2 = 450$ Hz; (e) $\bar{\Omega}_2 = 525$ Hz; (f) $\bar{\Omega}_2 = 600$ Hz; (g) $L_2^* = 0$in Eq. (33).

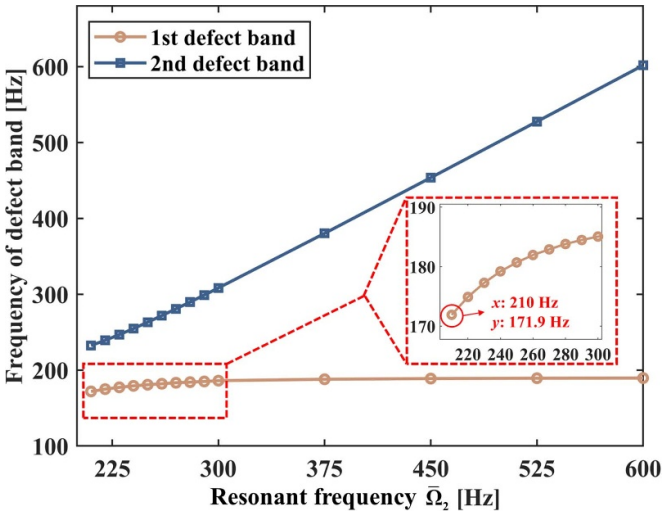

Figure 14. Evolution of defect band frequencies with varying $\bar{\Omega}_2$, where $\bar{\Omega}_1$is fixed at 200 Hz.

when the resonant frequencies are very close, the interaction between the loops becomes more significant, and the resonating loop no longer behaves as an isolated system. As a result, an optimization problem arises in the decoupled tuning of defect modes. Multi-objective optimization methods, such as genetic algorithms, could be employed to tune the circuit parameters, ensuring minimal interference between circuit loops when resonant frequencies are close and preventing defect modes from disappearing due to narrow bandgaps. Since this is not the focus of the current work, it will not be further elaborated.

In addition to the band structure analysis, figures 15(a)–(c) shows the harmonic responses of the defective piezoelectric metamaterial for three sets of resonance frequencies, i.e. $\bar{\Omega}_1 = 200$ and $\bar{\Omega}_2 = 300$ Hz, $\bar{\Omega}_1 = 200$ and $\bar{\Omega}_2 = 450$ Hz, $\bar{\Omega}_1 = 200$ and $\bar{\Omega}_2 = 600$ Hz, which correspond to (b), (d), and (f) in figure 13, respectively. It is found that the SEM and COMSOL results show high consistency, validating the accuracy of the proposed model. In the enlarged view of the bandgap in figures 15(a)–(c), the defect-mode frequencies Ω_{defect} appear as peaks, labeled A-F. To distinguish the energy localization properties of the second defect band from those of the first, figure 15(d) shows the contours of normalized wave mode shapes corresponding to Ω_{defect} as identified in figures 15(a)–(c). Notably, as $\bar{\Omega}_2$ varies, the normalized wave mode shape of the 1st defect band remains unchanged, as illustrated by A, C, and E in figure 15(d), indicating no interference between the two defect modes. In addition, when $\bar{\Omega}_2$ is relatively close to $\bar{\Omega}_1$, e.g. $\bar{\Omega}_1 = 200$ and $\bar{\Omega}_2 = 300$ Hz, the mode shapes of the two defect bands resemble each other, as shown by A and B in figure 15(d). However, with increasing $\bar{\Omega}_2$, the energy localization effect of the 2nd defect band gradually diminishes, as observed in D and F in figure 15(d). The above phenomenon further substantiates that the wave localization properties of defect modes in piezoelectric metamaterials are frequency dependent, with the localization effect diminishing as frequency increases.

Figure 16 presents the contours of the normalized wave mode shape as a function of frequency for the defective piezoelectric metamaterial beams at $\bar{\Omega}_1 = 200$ and $\bar{\Omega}_2 = 300$ Hz, serving to illustrate details of the defect modes in frequency-space. Within the frequency ranges of 182–186 Hz and 305–309 Hz, two vibration suppression regions are observed, corresponding to BG1 and BG2, respectively. The enlarged views show significant vibrations at the central position (i.e. $x/kd = 0.5$) of the piezoelectric metamaterial beam within BG1 and BG2, indicating the wave localization. The 1st and 2nd defect-mode frequencies Ω_{defect} are also highlighted in the enlarged views.

Thus far, the results of this section validate the conjecture in section 2.2, demonstrating that arbitrary decoupled defect

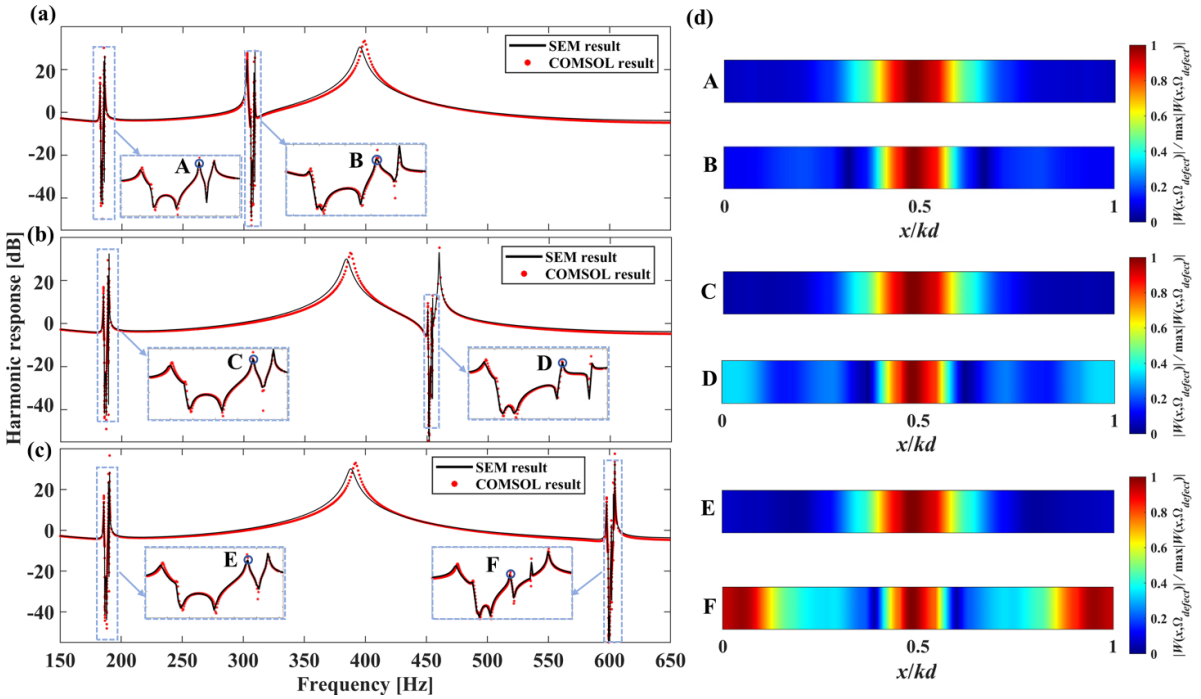

Figure 15. Harmonic responses of the defective piezoelectric metamaterial beams consisting of 11 unit cells for the cases of (a) $\bar{\Omega}_1 = 200$, $\bar{\Omega}_2 = 300$ Hz; (b) $\bar{\Omega}_1 = 200$, $\bar{\Omega}_2 = 450$ Hz; and (c) $\bar{\Omega}_1 = 200$, $\bar{\Omega}_2 = 600$ Hz. The black solid curve and red asterisk are SEM and COMSOL results, respectively. Defect-mode frequencies Ω_{defect} are labeled A-F within the enlarged view of the bandgap regions. Contours of normalized wave mode shapes corresponding to the identified Ω_{defect} are shown in (d).

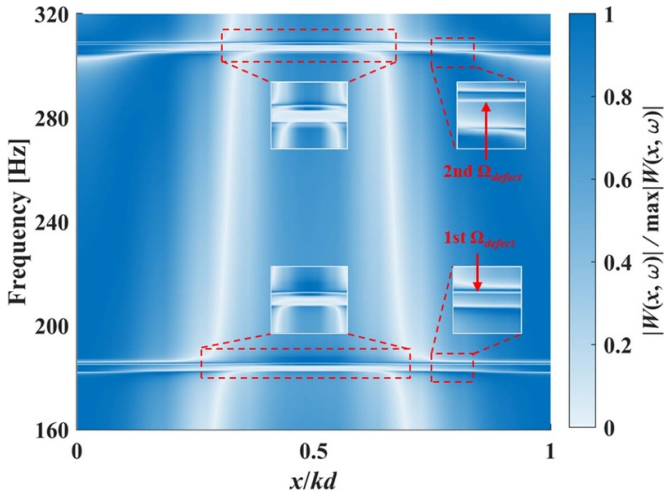

Figure 16. Contours of the normalized wave mode shape as a function of frequency for defective piezoelectric metamaterial beams at $\bar{\Omega}_1 = 200$ and $\bar{\Omega}_2 = 300$ Hz.

modes can be generated in multiple bandgaps. This approach fundamentally differs from existing methods for broadening defect modes. Specifically, traditional techniques such as dual defects or grading defects create multiple defect modes by introducing additional defects through modifying geometries, materials, or circuit parameters at different spatial locations in the metamaterial. However, these methods usually result in coupled defect modes, where changes to defect parameters simultaneously affect all defect-mode frequencies and the wave localization effect. Additionally, the multiple defect bands produced by these methods are typically formed within a single bandgap, limiting their frequency tuning range. In contrast, the method proposed in this work requires no spatially distributed defects. Instead, it enables multiple independently tunable defect modes through the adjustment of circuit parameters. Another advantage is that the defect bands are formed in different bandgaps and are therefore theoretically tunable to arbitrary frequency.

To further validate the proposed approach, additional examples are presented to demonstrate its capability to achieve arbitrary decoupled defect modes across multiple frequency bands. Without loss of generality, three higher-order circuit configurations are examined: circuit order $n = 4$ (Case 1), $n = 6$ (Case 2), and $n = 8$ (Case 3), designed to generate four, six, and eight LR bandgaps, respectively. In Case 3, the desired resonance frequencies are specified as $\bar{\Omega}_1 = 250$, $\bar{\Omega}_2 = 280$, $\bar{\Omega}_3 = 310$, $\bar{\Omega}_4 = 340$, $\bar{\Omega}_5 = 370$, $\bar{\Omega}_6 = 400$, $\bar{\Omega}_7 = 430$ and $\bar{\Omega}_8 = 460$ Hz. The desired resonance frequencies for Cases 1 and 2 are taken from the first four and first six resonance frequencies specified in Case 3, respectively. Based on the analysis in section 4, to ensure the decoupling of the defect modes, the capacitance C_1 in the circuit for all three cases is set to 100 nF, while the other capacitances in these cases are set to 1 nF. All other geometric and material parameters remain consistent with the previous analysis. Figures 17(a)–(c) illustrates the band structures of the defective piezoelectric metamaterial shunted with C-F higher-order resonant circuit for $n = 4$, $n = 6$, and $n = 8$, respectively. In figure 17(a), four defect bands corresponding to the desired frequencies

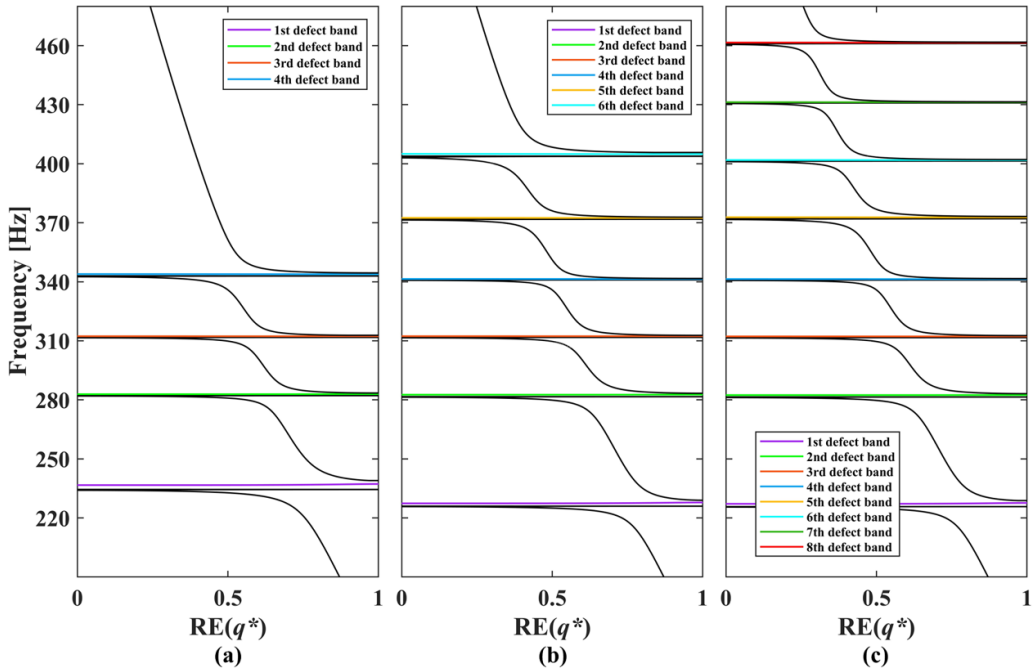

Figure 17. Band structures of the defective piezoelectric metamaterial incorporating C-F higher-order resonant circuit for varying circuit orders: (a) $n = 4$ (Case 1); (b) $n = 6$ (Case 2); (c) $n = 8$ (Case 3). Defect bands in different band gaps are highlighted with distinct colors.

appear, indicated by the colored lines. With increasing the circuit order, as shown in figures 17(b) and (c), additional defect bands emerge at the designated frequencies. Except for the 1st defect band, the frequencies of the other existing defect bands remain largely unaffected. The shift in the 1st defect band frequency is due to the non-ideal switching characteristics of the current-flowing branch in the C-F higher-order resonant circuit caused by $C_1 = 100$ nF, similar to the case discussed in figure 13(a).

6. Conclusions

This paper addresses the challenge of achieving multi-band wave localization with a single spatial defect by introducing electrically controlled defects. A new type of defective piezoelectric metamaterial beam is proposed, comprising periodically arranged piezoelectric elements, each shunted to a C-F higher-order resonant circuit. One cell is selectively coupled to a first-order resonant circuit, thereby creating an electrically controlled defect. The advantage of C-F higher-order resonant circuits lies in the ability of their 'current-flowing' branches to exhibit a 'switching' characteristic across different resonant frequencies, enabling independent operation of resonant branches. Building on this property, we propose a multi-bandgap decoupling tuning method to realize the arbitrary decoupled defect modes. To enhance computational efficiency and prediction accuracy, the band structure of the proposed design is calculated using the spectral transfer matrix method in conjunction with the supercell technique, while the harmonic response is obtained using the SEM. The study yields several valuable conclusions. First, the energy-localized behavior is most pronounced when the circuit condition at the defect is either open or short-circuited. This localization effect is frequency-dependent, diminishing as the defect-mode frequency increases. Second, by increasing the order of the C-F higher-order resonant circuits, an arbitrary number of defect modes can be generated at desired frequencies. Third, the resulting multiple defect modes are effectively decoupled in terms of frequency and wave localization strength. Compared to traditional defect metamaterials, the proposed design eliminates the reliance of defect mode formation on physical structural defects. It provides greater flexibility in adjusting the spatial localization, frequency, and number of defect modes generated. Additionally, it is recommended to employ programmable digital circuits technology for the implementation of the circuits in this study. This technology not only addresses the parasitic resistance issues associated with traditional synthetic circuits but also has the potential to realize adaptive defect modes, positioning the design as a promising solution for waveguides and sensor devices operating in complex and dynamic vibration environments.

Data availability statement

All data that support the findings of this study are included within the article (and any supplementary files).

Acknowledgment

Yupei Jian would like to gratefully acknowledge the Sichuan Science and Technology Program (Grant No. 2025ZNSFSC1268), the China Postdoctoral Science Foundation (Grant No. 2024M762677), and the Fundamental

Research Funds for the Central Universities (Grant No. 2682024CX026). Hesheng Han thanks the support from the Shenzhen Science and Technology Program (Grant No. RCBS20231211090558094), and the National Natural Science Foundation of China (Grant No. 12302030) for financial support. Guobiao Hu would like to gratefully acknowledge the National Natural Science Foundation of China (Grant No. 52305135) and the Guangzhou Municipal Science and Technology Bureau (Grant Nos. SL2023A03J00869, SL2023A04J01741) for their financial support.

Conflict of interest

We declare that there is no conflict of interest between the authors.

ORCID iDs

Yupei Jian https://orcid.org/0000-0002-8094-0769
Lihua Tang https://orcid.org/0000-0001-9031-4190
Weiqun Liu https://orcid.org/0000-0002-0843-903X
Guobiao Hu https://orcid.org/0000-0002-1288-7564

References

[1] Guo Z, Jiang S, Shen Y, Jiang G, Xiao B, Xu Q and Li M 2025 Nonlinear dynamic analysis and vibration reduction of two sandwich beams connected by a joint with clearance *Mech. Syst. Signal Process.* **223** 111828
[2] Vasileiadis T, Varghese J, Babacic V, Gomis-Bresco J, Navarro Urrios D and Graczykowski B 2021 Progress and perspectives on phononic crystals *J. Phys. D: Appl. Phys.* **129** 160901
[3] Wang L, Zheng H, Zhao M, Shi L and Hou S 2021 Petrov–Galerkin method for the band structure computation of anisotropic and piezoelectric phononic crystals *Appl. Math. Modelling* **89** 1090–105
[4] Yang S, Chang H, Wang Y, Yang M and Sun T 2024 A phononic crystal suspension for vibration isolation of acoustic loads in underwater gliders *Appl. Acoust.* **216** 109731
[5] Wu X, Li X, Qi P, Zhang C and Luo J 2024 Experimental design and adaptive modulation of piezoelectric cantilever phononic crystals for vibration attenuation in vehicle subframes *Smart Mater. Struct.* **33** 025026
[6] Wan B-F, Zhou Z-W, Xu Y and Zhang H-F 2020 A theoretical proposal for a refractive index and angle sensor based on one-dimensional photonic crystals *IEEE Sens. J.* **21** 331–8
[7] Zhang X, Li Y, Wang Y, Jia Z and Luo Y 2021 Narrow-band filter design of phononic crystals with periodic point defects via topology optimization *Int. J. Mech. Sci.* **212** 106829
[8] Xiao J, Ding X, Huang W, He Q and Shao Y 2024 Rotating machinery weak fault features enhancement via line-defect phononic crystal sensing *Mech. Syst. Signal Process.* **220** 111657
[9] Zhu T, Jiang M, Wang Y-F and Wang Y-S 2024 Reconfigurable inverse design of phononic crystal sensor based on a deep learning accelerated evolution strategy *Thin-Walled Struct.* **204** 112255
[10] Moctezuma-Enriquez D, Rodriguez-Viveros Y, Manzanares-Martinez M, Castro-Garay P, Urrutia-Banuelos E and Manzanares-Martinez J 2011 Existence of a giant hypersonic elastic mirror in porous silicon superlattices *Appl. Phys. Lett.* **99** 171901
[11] Lin X, Li E, He Z, Wu Y and Li Q 2021 Design of single-phase chiral metamaterials for broadband double negativity via shape optimization *Appl. Math. Modelling* **91** 335–57
[12] Akbari-Farahani F and Ebrahimi-Nejad S 2023 From defect mode to topological metamaterials: a state-of-the-art review of phononic crystals & acoustic metamaterials for energy harvesting *Sens. Actuators* A **365** 114871
[13] Lin Z-K, Wang Q, Liu Y, Xue H, Zhang B, Chong Y and Jiang J-H 2023 Topological phenomena at defects in acoustic, photonic and solid-state lattices *Nat. Rev. Phys.* **5** 483–95
[14] Oudich M, Gerard N J, Deng Y and Jing Y 2023 Tailoring structure-borne sound through bandgap engineering in phononic crystals and metamaterials: a comprehensive review *Adv. Funct. Mater.* **33** 2206309
[15] Zhang G-Y, Liu Z-J, Li B-Z, Dou X-L, Zhang C-R, Sun X-W and Yang Y-M 2024 Phononic crystals with incomplete line defects: applications in high-performance and broadband acoustic energy localization and harvesting *Smart Mater. Struct.* **33** 085036
[16] Shelke A, Banerjee S, Habib A, Rahani E K, Ahmed R and Kundu T 2014 Wave guiding and wave modulation using phononic crystal defects *J. Intell. Mater. Syst. Struct.* **25** 1541–52
[17] Shao H, Chen G and He H 2021 Elastic wave localization and energy harvesting defined by piezoelectric patches on phononic crystal waveguide *Phys. Lett.* A **403** 127366
[18] Park C-S, Shin Y C, Jo S-H, Yoon H, Choi W, Youn B D and Kim M 2019 Two-dimensional octagonal phononic crystals for highly dense piezoelectric energy harvesting *Nano Energy* **57** 327–37
[19] Lee D, Youn B D and Jo S-H 2023 Deep-learning-based framework for inverse design of a defective phononic crystal for narrowband filtering *Int. J. Mech. Sci.* **255** 108474
[20] Li X, Qin Y, He G, Lian F, Zuo S and Cai C 2023 Machine learning-assisted inverse design of wide-bandgap acoustic topological devices *J. Appl. Phys.* **57** 135303
[21] Chen J, Huang J, An M, Hu P, Xie Y, Wu J and Chen Y 2024 Application of machine learning on the design of acoustic metamaterials and phonon crystals: a review *Smart Mater. Struct.* **33** 073001
[22] Jian Y, Tang L, Hu G, Wang Y and Aw K C 2022 Adaptive genetic algorithm enabled tailoring of piezoelectric metamaterials for optimal vibration attenuation *Smart Mater. Struct.* **31** 075026
[23] Hu G, Tang L, Liang J, Lan C and Das R 2021 Acoustic-elastic metamaterials and phononic crystals for energy harvesting: a review *Smart Mater. Struct.* **30** 085025
[24] Oudich M and Li Y 2017 Tunable sub-wavelength acoustic energy harvesting with a metamaterial plate *J. Phys. D: Appl. Phys.* **50** 315104
[25] Katch L, Moghaddaszadeh M, Willey C, Juhl A, Nouh M and Argüelles A 2023 Analysis of geometric defects in square locally resonant phononic crystals: a comparative study of modeling approaches *J. Acoust. Soc. Am.* **154** 3052–61
[26] Cao D-X, Li S-S, Zhan C-H, Lu Y-M, Mao J-J and Lai S-K 2022 Defect-mode-induced energy localization/harvesting of a locally resonant phononic crystal plate: analysis of line defects *J. Infrastruct. Intell. Resilience* **1** 100001
[27] Ma K, Tan T, Yan Z, Liu F, Liao W-H and Zhang W 2021 Metamaterial and Helmholtz coupled resonator for high-density acoustic energy harvesting *Nano Energy* **82** 105693
[28] Li T, Wang Z, Xiao H, Yan Z, Yang C and Tan T 2021 Dual-band piezoelectric acoustic energy harvesting by

structural and local resonances of Helmholtz metamaterial *Nano Energy* **90** 106523
[29] Jo S-H and Youn B D 2021 An improved analytical model that considers lateral effects of a phononic crystal with a piezoelectric defect for elastic wave energy harvesting *Int. J. Mech. Sci.* **205** 106593
[30] He Z, Zhang G, Chen X, Cong Y, Gu S and Hong J 2023 Elastic wave harvesting in piezoelectric-defect-introduced phononic crystal microplates *Int. J. Mech. Sci.* **239** 107892
[31] Jian Y, Hu G, Tang L, Xu J, Huang D and Aw K 2024 Graded metamaterial with broadband active controllability for low-frequency vibration suppression *J. Appl. Phys.* **136** 043108
[32] Kaina N, Causier A, Bourlier Y, Fink M, Berthelot T and Lerosey G 2017 Slow waves in locally resonant metamaterials line defect waveguides *Sci. Rep.* **7** 15105
[33] Kiyota K, Kise T, Yokouchi N, Ide T and Baba T 2006 Various low group velocity effects in photonic crystal line defect waveguides and their demonstration by laser oscillation *Appl. Phys. Lett.* **88** 201904
[34] Jo S-H, Shin Y C, Choi W, Yoon H, Youn B D and Kim M 2021 Double defects-induced elastic wave coupling and energy localization in a phononic crystal *Nano Converg.* **8** 27
[35] Jo S-H, Yoon H, Shin Y C and Youn B D 2020 A graded phononic crystal with decoupled double defects for broadband energy localization *Int. J. Mech. Sci.* **183** 105833
[36] Xiao H, Tan T, Li T, Zhang L, Yuan C and Yan Z 2023 Enhanced multi-band acoustic energy harvesting using double defect modes of Helmholtz resonant metamaterial *Smart Mater. Struct.* **32** 105030
[37] Huang B, Sun M and Peng D 2018 Intrinsic energy conversions for photon-generation in piezo-phototronic materials: a case study on alkaline niobates *Nano Energy* **47** 150–71
[38] Ying C, Jing D, Jia S, Qiguang Z and Weihong B 2015 Study on tunable filtering performance of compound defect photonic crystal with magnetic control *Optik* **126** 5353–6
[39] Geng Q, Wang T, Wu L and Li Y 2021 Defect coupling behavior and flexural wave energy harvesting of phononic crystal beams with double defects in thermal environments *J. Appl. Phys.* **54** 225501
[40] Deng T, Zhang S and Gao Y 2019 A magnetic-dependent vibration energy harvester based on the tunable point defect in 2D magneto-elastic phononic crystals *Crystals* **9** 261
[41] Jo S-H, Park M, Kim M and Yang J 2024 Tunable bandpass filters using a defective phononic crystal shunted to synthetic negative capacitance for longitudinal waves *J. Appl. Phys.* **135** 164502
[42] Thomes R L, Beli D and Junior C D M 2022 Space-time wave localization in electromechanical metamaterial beams with programmable defects *Mech. Syst. Signal Process.* **167** 108550
[43] Jian Y, Hu G, Tang L, Tang W, Abdi M and Aw K C 2023 Analytical and experimental study of a metamaterial beam with grading piezoelectric transducers for vibration attenuation band widening *Eng. Struct.* **275** 115091
[44] Yang F, Sedaghati R and Esmailzadeh E 2022 Vibration suppression of structures using tuned mass damper technology: a state-of-the-art review *J. Vib. Control* **28** 812–36
[45] Fleming A, Behrens S and Moheimani S 2003 Reducing the inductance requirements of piezoelectric shunt damping systems *Smart Mater. Struct.* **12** 57
[46] Zhou W, Wu Y and Zuo L 2015 Vibration and wave propagation attenuation for metamaterials by periodic piezoelectric arrays with high-order resonant circuit shunts *Smart Mater. Struct.* **24** 065021
[47] Adriaens H, De Koning W L and Banning R 2000 Modeling piezoelectric actuators *IEEE/ASME Trans. Mechatronics* **5** 331–41
[48] Sugino C, Leadenham S, Ruzzene M and Erturk A 2017 An investigation of electroelastic bandgap formation in locally resonant piezoelectric metastructures *Smart Mater. Struct.* **26** 055029
[49] Lee U, Kim D and Park I 2013 Dynamic modeling and analysis of the PZT-bonded composite Timoshenko beams: spectral element method *J. Sound Vib.* **332** 1585–609
[50] Hu G, Tang L, Yang Y, Yu D and Zi Y 2023 High-fidelity dynamics of piezoelectric covered metamaterial timoshenko beams using the spectral element method *Smart Mater. Struct.* **32** 095023
[51] Guo Z, Wen J, Shen Y, Hu G and Jiang G 2024 Band folding induced broadband vibration suppression of star-shaped metamaterials: theory and experiment *Thin-Walled Struct.* **198** 111756
[52] De Moura B, Machado M, Dey S and Mukhopadhyay T 2024 Manipulating flexural waves to enhance the broadband vibration mitigation through inducing programmed disorder on smart rainbow metamaterials *Appl. Math. Modelling* **125** 650–71
[53] Erturk A and Inman D J 2008 A distributed parameter electromechanical model for cantilevered piezoelectric energy harvesters *J. Vib. Acoust.* **130** 041002–1
[54] Liu X, Hu G, Sun C and Huang G 2011 Wave propagation characterization and design of two-dimensional elastic chiral metacomposite *J. Sound Vib.* **330** 2536–53
[55] Zhong W and Williams F 1995 On the direct solution of wave propagation for repetitive structures *J. Sound Vib.* **181** 485–501
[56] Fabro A T, Meng H and Chronopoulos D 2020 Uncertainties in the attenuation performance of a multi-frequency metastructure from additive manufacturing *Mech. Syst. Signal Process.* **138** 106557
[57] Jian Y, Hu G, Tang L, Shen Y, Zhan Y and Aw K 2023 Adaptive piezoelectric metamaterial beam: autonomous attenuation zone adjustment in complex vibration environments *Smart Mater. Struct.* **32** 105023
[58] Cruz M, Beltrán M, Wang C, Tagüeña-Martínez J and Rubo Y G 1999 Supercell approach to the optical properties of porous silicon *Phys. Rev.* B **59** 15381
[59] Sugino C, Alshaqaq M and Erturk A 2022 Spatially programmable wave compression and signal enhancement in a piezoelectric metamaterial waveguide *Phys. Rev.* B **106** 174304
[60] Jian Y, Tang L, Hu G, Li Z and Aw K C 2022 Design of graded piezoelectric metamaterial beam with spatial variation of electrodes *Int. J. Mech. Sci.* **218** 107068
[61] Berardengo M, Manzoni S, Thomas O and Vanali M 2018 Piezoelectric resonant shunt enhancement by negative capacitances: optimisation, performance and resonance cancellation *J. Intell. Mater. Syst. Struct.* **29** 2581–606
[62] Alshaqaq M, Sugino C and Erturk A 2023 Digital programming of reciprocity breaking in resonant piezoelectric metamaterials *Phys. Rev. Res.* **5** 043003
[63] Yi K, Matten G, Ouisse M, Sadoulet-Reboul E, Collet M and Chevallier G 2020 Programmable metamaterials with digital synthetic impedance circuits for vibration control *Smart Mater. Struct.* **29** 035005
[64] Tang W, Chen Z, Cui M and Li Z 2024 Active piezoelectric metamaterials with model-free controller for large low-frequency vibration attenuation *IEEE/ASME Trans. Mechatronics* **29** 3845–55